The MJO and Air–Sea Interaction in TOGA COARE and DYNAMO

SIMON P. DE SZOEKE

College of Earth, Ocean, and Atmospheric Science, Oregon State University, Corvallis, Oregon

JAMES B. EDSON

University of Connecticut, Groton, Connecticut

JUNE R. MARION

College of Earth, Ocean, and Atmospheric Science, Oregon State University, Corvallis, Oregon

CHRISTOPHER W. FAIRALL AND LUDOVIC BARITEAU

Physical Sciences Division, NOAA/Earth System Research Laboratory, Boulder, Colorado

(Manuscript received 4 July 2014, in final form 9 October 2014)

ABSTRACT

Dynamics of the Madden–Julian Oscillation (DYNAMO) and Tropical Ocean and Global Atmosphere Coupled Ocean–Atmosphere Response Experiment (TOGA COARE) observations and reanalysis-based surface flux products are used to test theories of atmosphere–ocean interaction that explain the Madden–Julian oscillation (MJO). Negative intraseasonal outgoing longwave radiation, indicating deep convective clouds, is in phase with increased surface wind stress, decreased solar heating, and increased surface turbulent heat flux—mostly evaporation—from the ocean to the atmosphere. Net heat flux cools the upper ocean in the convective phase. Sea surface temperature (SST) warms during the suppressed phase, reaching a maximum before the onset of MJO convection. The timing of convection, surface flux, and SST is consistent from the central Indian Ocean (70°E) to the western Pacific Ocean (160°E).

Mean surface evaporation observed in TOGA COARE and DYNAMO (110 W m^{-2}) accounts for about half of the moisture supply for the mean precipitation (210 W m^{-2} for DYNAMO). Precipitation maxima are an order of magnitude larger than evaporation anomalies, requiring moisture convergence in the mean, and on intraseasonal and daily time scales. Column-integrated moisture increases 2 cm before the convectively active phase over the Research Vessel (R/V) *Roger Revelle* in DYNAMO, in accordance with MJO moisture recharge theory. Local surface evaporation does not significantly recharge the column water budget before convection. As suggested in moisture mode theories, evaporation increases the moist static energy of the column during convection. Rather than simply discharging moisture from the column, the strongest daily precipitation anomalies in the convectively active phase accompany the increasing column moisture.

1. Introduction

The Madden–Julian oscillation (MJO) is the leading intraseasonal (30–60 day) mode of atmospheric variability of the equatorial atmosphere [Madden and Julian (1971), reviewed in Waliser (2006)]. It comprises alternating zonal wind anomalies in the lower and upper troposphere of the planetary zonal scale. Deep convection accompanies surface convergence and upper-level divergence, and suppressed convection accompanies surface divergence. The 30–60-day time scale of the MJO is long compared to the time scale of atmospheric convection, and it propagates eastward at 5 m s^{-1}.

The long time scale of the MJO and its slow propagation compared to the observed time scales of atmospheric

Corresponding author address: Simon P. de Szoeke, College of Earth, Ocean, and Atmospheric Science, Oregon State University, 104 CEOAS Admin. Building, Corvallis, OR 97331.
E-mail: sdeszoek@coas.oregonstate.edu

DOI: 10.1175/JCLI-D-14-00477.1

convection and propagation speeds of equatorial waves remains unexplained by theoretical models. Most commonly cited models explain low-level convergence by unbalanced diabatic heating by convection [wave-conditional instability of the second kind (CISK); (e.g., Gill 1980; Lau and Peng 1987) or boundary layer frictional wave-CISK (e.g., Wang and Rui 1990; Salby et al. 1994)] or by a quasi-equilibrium between circulation and radiative-convective equilibrium (Neelin et al. 1987; Emanuel 1987; Neelin and Zeng 2000). Other models with nonlinear interaction of smaller-scale waves (e.g., through triggering convection) predict organization of synoptic-scale convection into a large MJO envelope (Majda and Stechmann 2009; Yang and Ingersoll 2013). The waves predicted by wave-CISK propagate faster than the MJO, and the shortest waves are the most unstable to wave-CISK (Hendon 2005). Frictional wave-CISK predicts slower waves destabilized by boundary layer moist static energy convergence. Convectively coupled equatorial Kelvin, Rossby, and inertia–gravity waves are observed with higher frequencies and smaller scales that do not match the planetary scale of the MJO (Wheeler and Kiladis 1999).

Quasi-equilibrium models assume that latent heating above precipitation is balanced by adiabatic cooling of buoyant rising air (e.g., Riehl and Malkus 1958), and convection quickly redistributes moist static energy anomalies from the boundary layer throughout the troposphere to an equilibrium temperature profile. Neelin et al. (1987) and Emanuel (1987) developed quasi-equilibrium models with wind–evaporation or wind-induced surface heat exchange (WISHE) to explain growth and eastward propagation of convective anomalies. In WISHE, evaporation from the ocean surface is enhanced under stronger wind speeds to the east of the maximum upward velocity anomaly for easterly mean winds. Contrary to the eastward propagation of the MJO, the original WISHE theory predicts westward propagation of disturbances for the mean westerlies found over the Indian Ocean and western Pacific.

Under weak planetary rotation (implying large Rossby radius of deformation) gravity waves efficiently redistribute temperature anomalies throughout the tropics. The resulting relatively homogeneous temperature structure observed in the tropical free troposphere is modeled by the weak temperature gradient (WTG) assumption (Sobel and Bretherton 2000; Sobel et al. 2001). Even in the case of weak temperature gradients, moisture anomalies increase the moist static energy of the tropospheric column (e.g., Maloney 2009). ''Moisture mode'' theories for the MJO consider the feedback between moisture anomalies and convection (Sugiyama 2009; Hannah and Maloney 2014; Benedict et al. 2014). The quasi-equilibrium moisture mode grows when there is an alignment between precipitation and net column heating.

No single theory has been accepted that links tropical convection and large-scale equatorial waves yielding anomalies on the time and spatial scale of the MJO. It has been suggested that the thermal inertia of the upper ocean may play a role in setting the intraseasonal time scale and slow propagation of the MJO (e.g., Krishnamurti et al. 1988). Although MJO variability is found in some uncoupled simulations from atmospheric general circulation models, in many models coupled SST makes intraseasonal anomalies more closely resemble observed intraseasonal variability (Flatau et al. 1997; Waliser et al. 1999; Inness and Slingo 2003; Benedict and Randall 2011; DeMott et al. 2014). Atmospheric GCMs coupled to SST in slab ocean models improve predictability of intraseasonal variability compared to atmosphere-only general circulation models (Woolnough et al. 2007).

Intraseasonal air–sea interaction plays an important role on the stage of the warm pool of the Indian and Pacific Oceans (SST $>$ 28.5°C, Fig. 1a). The standard deviation of intraseasonal outgoing longwave radiation (OLR) anomalies contoured in Fig. 1a has maxima over both the Indian Ocean and western Pacific Ocean sectors of the warm pool, with lower amplitude over the Maritime Continent, particularly over the islands. Although the intraseasonal variability of zonal wind stress (Fig. 1b) is larger away from the equator, it also has two saddles of high variability bridging the equator to the east and west of the Maritime Continent. Figure 1b shows annual wind stress climatology from the Scatterometer Climatology of Ocean Winds (SCOW; Risien and Chelton 2008) as vectors. The zonal wind stress is shaded. The zonal wind stress is westward throughout most of the tropics, but high intraseasonal variability in zonal wind stress and convection coincides with regions of warm SST and eastward mean winds near the equator. Locations of Dynamics of the Madden–Julian Oscillation (DYNAMO; Yoneyama et al. 2013) in the central Indian Ocean, and Tropical Ocean and Global Atmosphere Coupled Ocean–Atmosphere Response Experiment (TOGA COARE; Webster and Lukas 1992) in the western Pacific Ocean, are marked with stars in Fig. 1.

Three MJO convective events and their accompanying air–sea interactions were observed in TOGA COARE in 1992. Analyses of TOGA COARE observations and composites from reanalysis data showed wind speed and evaporation anomalies following OLR anomalies that indicate deep convection (Hendon and Glick 1997;

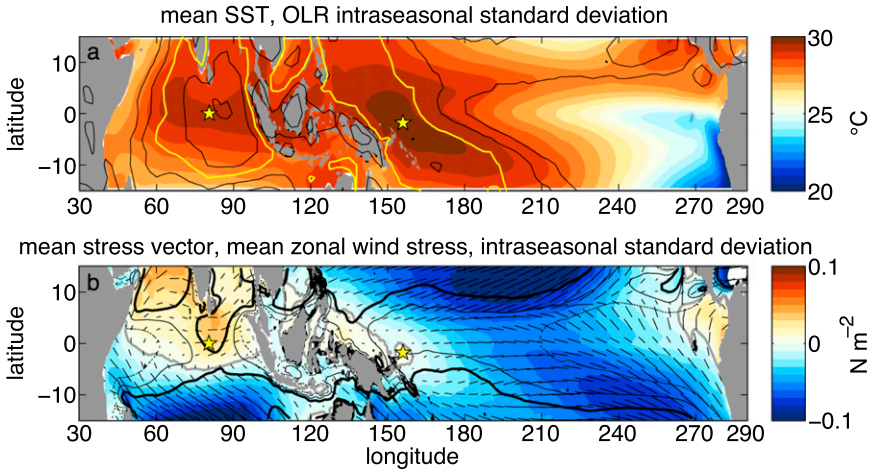

FIG. 1. (a) Mean SST for the equatorial Indian and Pacific Oceans (shaded) overlain by standard deviation of intraseasonal (15–100 day) OLR anomalies [black, contours above 15 W m^{-2} are shown with a contour interval of 3 W m^{-2}, yellow contour is 21 W m^{-2}]. (b) Zonal wind stress (shaded) and wind stress vectors from SCOW. The zero zonal wind stress contour is gray. The standard deviation of intraseasonal zonal wind stress is contoured at 0.015 (dashed), 0.02 (light), and 0.025 (thick) N m^{-2}. Locations of DYNAMO (80.5°E) and TOGA COARE (156°E) ship observations used in this paper are marked with yellow stars.

Shinoda et al. 1998; Woolnough et al. 2000). Longer in situ records from Tropical Atmosphere Ocean (TAO) buoys show westerly wind bursts and evaporation considerably more synchronous with convection on average than was found for the reanalyses or the three events of TOGA COARE (Zhang and McPhaden 2000). SST decreased beneath the increased evaporative cooling and reduced solar radiation on the ocean surface. Though evaporation was enhanced in convective events, peak precipitation in convective events was 3–5 times greater than the rate of surface evaporation in TOGA COARE (Lin and Johnson 1996), with moisture convergence supplying most of the moisture for the precipitation.

We observed equatorial intraseasonal air–sea interaction in the central Indian Ocean during DYNAMO. In this paper we assess the response of surface fluxes and SST to intraseasonal convective anomalies, examining the evidence that intraseasonal interaction of the atmosphere with surface fluxes, or with the SST, is a significant contributor to the MJO. We use TOGA COARE and DYNAMO observations, and surface flux products based on global reanalyses. From these datasets we assess three hypothetical models of ocean–atmosphere interactions:

1) Intraseasonal surface flux feedback: Intraseasonal atmospheric variability, primarily wind speed and clouds, affects surface heat fluxes (mostly evaporation), contributing to boundary layer moist static energy fluctuations that destabilize the atmosphere to intraseasonal convective modes (which might be wave-CISK, or frictional wave-CISK, or moisture modes). In this process, surface fluxes are modulated by intraseasonally changing meteorological variables, whether or not the ocean responds to the changing conditions (Neelin et al. 1987; Emanuel 1987; Weller and Anderson 1996; Sugiyama 2009; Sobel et al. 2010; Sobel and Maloney 2012).
2) Coupled ocean–atmosphere interaction: Intraseasonal atmospheric variability modifies sea surface temperature (SST) and ocean mixed layer depth. Intraseasonal changes in the wind strongly modulate the surface fluxes, ocean mixing, mixed layer depth, and heat storage by the ocean. The heat stored in the upper ocean affects surface fluxes and feeds back to atmospheric convection (Hendon and Glick 1997; Wang and Xie 1998; Woolnough et al. 2000; Inness and Slingo 2003; Marshall et al. 2008).
3) Atmospheric moisture recharge: Moisture builds up in the atmospheric column, particularly the lower free troposphere, in the convectively suppressed phase. This moisture preconditions the atmosphere for subsequent convective anomalies. Anomalous precipitation in the convectively active phase discharges moisture from the atmospheric column, suppressing convection until the column moisture can recharge again. Moisture recharge in the suppressed phase could be due to evaporation, horizontal convergence of water vapor, or vertical transport of moisture by shallow cumulus or cumulus congestus

clouds that detrain water in the midtroposphere (Bladé and Hartmann 1993; Johnson et al. 1999; Kemball-Cook and Weare 2001; Benedict and Randall 2009).

In section 2 we introduce the DYNAMO and TOGA COARE in situ observations and assess the OAFlux and TropFlux surface flux datasets against them. Appendix A provides a detailed description of each variable in DYNAMO surface meteorology and flux dataset from the Research Vessel (R/V) *Roger Revelle*. The methods used for isolating and compositing equatorial waves and the MJO are described in section 3, with more details in appendix B.

In section 4 we present observed time series of daily and subdaily variability from DYNAMO and TOGA COARE, and the analysis of 27 years of the daily time–longitude structure air–sea interaction variables and in relation to the MJO. Section 5 presents a discussion of the contribution of the surface flux and SST variation to MJO convective anomalies and section 6 concludes the paper.

2. Data

a. DYNAMO

We use in situ time series observations collected from the R/V *Roger Revelle* in the DYNAMO experiment intensive observation period. The DYNAMO–*Revelle* sampling consisted of four research cruises (Moum et al. 2014). We present the surface meteorology and air–sea flux data from legs 2–4 (3 October–31 December 2011) when the ship spent considerable time on the equator in the vicinity of 80.5°E.

Oregon State University, University of Connecticut (UConn), and the National Oceanic and Atmospheric Administration (NOAA)/Earth System Research Laboratory Physical Sciences Division (ESRL/PSD) deployed parallel surface meteorology and covariance flux systems on the forward mast of the *Revelle* [similar to shipboard systems described in Fairall et al. (1997)]. Together these systems measured mean air temperature, humidity (at 15 m above sea level), vector wind (~20 m), sea surface temperature at 0.1-m depth (SST), and downwelling solar and longwave infrared radiative fluxes each minute. The DYNAMO observations are described further in appendix A. Unless otherwise noted, in this paper we use 10-min averages of the DYNAMO surface meteorology and flux variables. Fluxes shown herein are computed from the 10-min averages with the COARE version 3.5 bulk aerodynamic formula (Fairall et al. 1996b; Fairall et al. 2003; Edson et al. 2013).

Meteorological, sea–air interface, and upper ocean variables are available in the DYNAMO–*Revelle* meteorology and flux group dataset [ftp://dynamo.dms.uconn.edu/ linked from the Earth Observatory Laboratory (EOL) field catalog http://data.eol.ucar.edu/master_list/?project=DYNAMO]. These variables and the techniques used to process them are further described in appendix A.

b. TOGA COARE

We use TOGA COARE observations from the R/V *Moana Wave* and Woods Hole Oceanographic Institution (WHOI) Improved Meteorological Packages (IMET) buoy [Weller and Anderson (1996); Anderson et al. (1996); available online at http://rda.ucar.edu/datasets/ds606.1/]. Similar data to the DYNAMO data described above were collected on the R/V *Moana Wave* (Fairall et al. 1997). Meteorological and oceanographic data from the IMET buoy were averaged hourly. Because precipitation is unevenly distributed and it is difficult to obtain a representative sample from single rain gauges, we use the average of gauges on the IMET buoy, the NOAA TAO buoy at 2°S, and the Research Vessels *Moana Wave* and *Wecoma* (Anderson et al. 1996).

c. Outgoing longwave radiation

Convectively coupled equatorial waves are diagnosed using principal component analysis and compositing using daily NOAA interpolated OLR data interpolated to 2.5° × 2.5° resolution [Liebmann and Smith (1996); available online at NOAA/ESRL/PSD http://www.esrl.noaa.gov/psd/data/gridded/data.interp_OLR.html]. We use the 27.5-yr period of data without gaps from January 1985 to June 2012. OLR data indicate the depth and/or frequency of deep convection. Daily data are suitable to diagnose intraseasonal MJO variability, convectively coupled equatorial Kelvin waves, and convectively coupled equatorial Rossby waves (Wheeler and Kiladis 1999).

d. TropFlux and OAFlux gridded surface flux products

We supplement the surface flux observations from DYNAMO and TOGA COARE with 1° × 1° spatially resolved air–sea fluxes for the global tropical oceans (TropFlux) and objectively analyzed air–sea fluxes (OAFlux) surface data. TropFlux (Praveen Kumar et al. 2012; http://www.incois.gov.in/tropflux/) uses bias-corrected European Centre for Medium-Range Weather Forecasts (ECMWF) Interim Re-Analysis (ERA-Interim, hereafter ERA-I) variables to compute fluxes. The SST, air temperature, air humidity, and wind speed variables from ERA-I were adjusted to remove biases compared to TAO, the Prediction and Research Moored Array in the Tropical Atlantic (PIRATA), and the Research

Moored Array for African–Asian–Australian Monsoon Analysis and Prediction (RAMA) buoy observations before computing fluxes with the COARE version 3.0 bulk flux algorithm. Neither the effect of the diurnal solar warm layer nor the effect of the cool viscous sublayer on SST are implemented in the TropFlux bulk flux computations.

OAFlux (Yu and Weller 2007) uses optimal analysis (OA) of two meteorological reanalysis products: the National Centers for Environmental Prediction–U.S. Department of Energy (NCEP–DOE) Reanalysis 2 (Kalnay et al. 1996; Kanamitsu et al. 2002) and the 40-yr ECMWF Re-Analysis (ERA-40; Uppala et al. 2005) and satellite SST and wind speed observations to provide inputs for the COARE 3.0 bulk flux algorithm. The optimal analysis of the flux input variables is found by minimizing a cost function of a weighted sum of differences between the analysis and model data and satellite observations. OAFlux uses in situ observations from buoys and ships collected in the Comprehensive Ocean–Atmosphere Data Set (COADS; Woodruff et al. 1998) to estimate the errors in the satellite and reanalysis estimates. In situ data from buoys and ship observations enter TropFlux and OAFlux through assimilation into the NCEP–DOE reanalysis, ERA-40, and ERA-I.

The intraseasonal (30–90 day) net surface heat flux standard deviation is about 20 W m^{-2} for either OAFlux or TropFlux over the Indian Ocean thermocline ridge [12°–5°S, 50°–80°E; Praveen Kumar et al. (2012), their Fig. 15c]. The daily gridded surface flux products agree well with in situ observations during DYNAMO and TOGA COARE. Figure 2 shows the agreement of daily latent and sensible heat flux with measurements made on board the R/V *Roger Revelle* in DYNAMO, and with the measurements on board the R/V *Moana Wave* in TOGA COARE. TropFlux and OAFlux overestimate TOGA COARE latent heat flux by 30 and 20 W m^{-2}, respectively. TropFlux underestimates the TOGA COARE mean sensible heat flux by 1 W m^{-2}.

The reanalyses used by the gridded flux products in Fig. 2 resolve the main features of daily variability. Daily TropFlux and OAFlux latent and sensible heat fluxes are correlated at 0.84 and 0.87, respectively, with the DYNAMO ship observations; and correlated 0.72 and 0.83, respectively, with the TOGA COARE ship observations. The success of TropFlux and OAFlux at reproducing the DYNAMO ship observations at 0°, 80.5°E may be due to the reanalyses assimilating data from the nearby RAMA buoy (0°, 80.5°E; ~2 km from the *Revelle*), and the slightly more distant RAMA buoys along 80.5°E at 1.5°S and 1.5°N. The standard deviation of the sensible heat flux is almost as large as the mean sensible

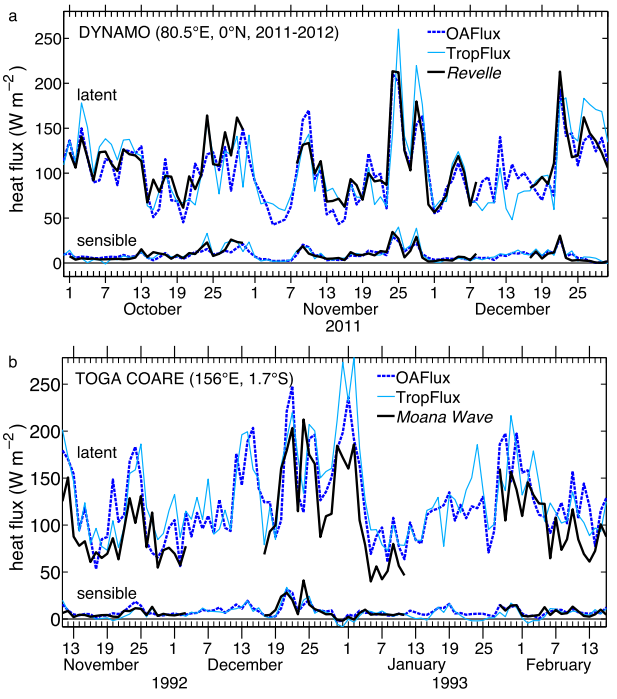

FIG. 2. TropFlux and OAFlux gridded surface flux products compared with ship observations (a) from the R/V *Roger Revelle* for DYNAMO in 2011 and (b) from the R/V *Moana Wave* for TOGA COARE in 1992/93.

heat flux (7–8 W m^{-2}). The standard deviation of TropFlux latent heat flux was 30 W m^{-2} for DYNAMO and 40 W m^{-2} for TOGA COARE. TropFlux and OAFlux overestimate the standard deviation of the latent heat flux by 14% and 8%, respectively, in TOGA COARE, and 20% and 8%, respectively, in DYNAMO. Mean sensible and latent heat fluxes, their standard deviations, and their correlation with the ship observations for DYNAMO are tabulated in Table 1.

Surface radiative fluxes are provided in OAFlux and TropFlux by the International Satellite Cloud Climatology Project (ISCCP) Flux Dataset (ISCCP FD; Zhang et al. 2004). TropFlux adjusts ISCCP FD for mean and amplitude biases relative to the buoy observations. Radiative surface fluxes from ISCCP FD match surface observations better than radiative fluxes from reanalysis. ISCCP FD is updated irregularly (available until 2009 at the time of writing), so TropFlux uses bias-corrected surface longwave fluxes from ERA-I reanalysis when ISCCP FD is not available. TropFlux "real time" solar radiation is derived as the ISCCP FD bias-corrected climatology plus an anomaly of 1.32 times the anomalous OLR (similar to Shinoda et al. 1998). Solar radiation derived in this way fits the mean and amplitude of surface observations well; however, it is clearly not independent of the OLR data.

TABLE 1. Comparison of OAFlux and TropFlux sensible (SHF) and latent (LHF) heat fluxes with R/V *Roger Revelle* surface flux observations.

	Mean ($W m^{-2}$)		Std dev ($W m^{-2}$)		*Revelle* correlation	
	LHF	SHF	LHF	SHF	LHF	SHF
R/V *Roger Revelle*	109.0	8.1	32.4	7.0	1	1
OAFlux	106.4	8.3	34.8	5.7	0.87	0.85
TropFlux	111.4	8.8	39.3	8.1	0.84	0.87

We also use the ERA-I (Dee et al. 2011) SST product provided with TropFlux on the $1° \times 1°$ grid. The ERA-I air temperature is consistent with this SST, according to the physics of the ERA-I model. ERA-I uses NCEP 7-day optimally interpolated SST (OISST; Reynolds et al. 2002) for 1989–2001 and daily Operational Sea Surface Temperature and Sea Ice Analysis (OSTIA; Donlon et al. 2012) from 2009 to the time of this writing.

3. Methods

We isolate intraseasonal variability in OLR, then composite the surface flux variables on the OLR-based index. We select symmetric MJO variability with a meridional average over 15°S–15°N. Intraseasonal variability is isolated from 27.5 yr (1985–2012) of continuous daily satellite OLR observations and the TropFlux and OAFlux surface fluxes with a sixth-order Butterworth bandpass filter with cutoff frequencies corresponding to periods of 15–100 days. We choose this relatively wide range of frequencies in order not to constrain the spectral characteristics of intraseasonal variability too narrowly.

Principal component analysis

We use principal component analysis (PCA) to isolate and diagnose the phase of the MJO (e.g., Shinoda et al. 1998; Wheeler and Hendon 2004; Kiladis et al. 2014). We perform PCA on the intraseasonally filtered ±15°N OLR time–longitude matrix. The PCA separates the time–longitude matrix into orthogonal spatial and temporal modes of variability. Each mode is separated into a spatial empirical orthogonal function (EOF; Figs. 3a–d) and a temporal principal component (PC) time series (Figs. 3e–h). Superposition of all modes recovers the entire time–longitude input data matrix. OLR varies most in the climatologically convective regions of the

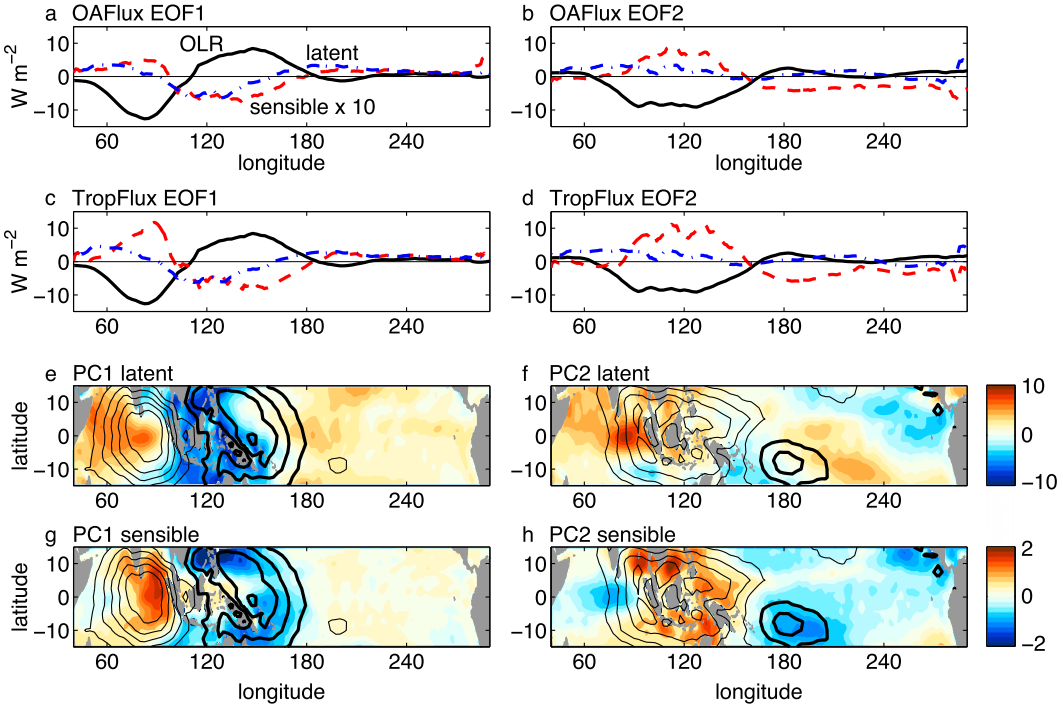

FIG. 3. The two leading EOFs of OLR averaged from 15°S to 15°N, and the regression of their PC time series onto the latent and sensible heat fluxes from (a),(b) OAFlux and (c),(d) TropFlux. Latent heat fluxes follow (are west of) sensible heat flux anomalies. Two-dimensional spatial pattern regressions on the first two PC time series for TropFlux (e),(f) latent heat flux and (g),(h) sensible heat flux (shaded). Positive heat flux anomalies indicate upward heat fluxes out of the ocean. Contours in (e)–(h) show the respective EOFs of OLR (contour interval of $2 W m^{-2}$).

Indian Ocean and western Pacific Ocean, so the PCA selects modes that explain variability in that region.

The first two principal components explain significantly more variance (21% and 16%) of the OLR data than the following principal components. The two PCs are nearly in quadrature, copropagating from west to east (Fig. 3). These two PCs are statistically distinct from the other PCs but not distinct from each other by the criterion of North et al. (1982). We retain only the first two PC time series as an efficient representation of eastward-propagating MJO events. The time–longitude structure of MJO is diagnosed by the product of the PC time series with the OLR EOFs, and with the spatial projections of the surface flux variables.

The truncated PC time series were normalized to have unity standard deviation, and the EOFs normalized so that they represent the spatial OLR pattern ($W\,m^{-2}$) projected for a normalized PC anomaly of 1. The surface wind stress, and sensible, latent, solar, and longwave heat fluxes were regressed onto the first two normalized PC time series to yield their spatial pattern (Figs. 3e–h).

The compositing procedure described in appendix B uses the phase of the MJO described by the angle of the vector formed from the first two principal components. The result of the analysis is essentially the same for OAFlux so we show only TropFlux for brevity.

4. Results

a. *Global and local intraseasonal variability of OLR and SST*

First we analyze the intraseasonal variability of OLR and SST during the DYNAMO (0°, 80.5°E, from October 2011 to January 2012) and TOGA COARE (1.8°S, 156°E, October 1992–March 1993) field experiments. Intraseasonal coupled atmosphere–ocean interaction ought to be reflected in variability of both atmospheric convection (OLR) and SST. Time series of daily OLR are traced by blue lines in Figs. 4a,c. Sea surface temperature time series from ERA-I (daily for DYNAMO and weekly for TOGA COARE) are shown in Figs. 4b,d. Intraseasonal (15–100-day filtered) variations of OLR and SST (thick blue lines, Fig. 4) indicate three local intraseasonal minima in OLR in the central Indian Ocean during DYNAMO. These minima of OLR, labeled I1, I2, and I3, indicate times when active convection drove cloud tops deep into the cold upper troposphere. These events were accompanied by decreasing SST and net upward surface heat flux, so that each minimum in OLR was followed by a minimum in SST within 2–10 days. Table 2 shows the dates of the identified intraseasonal events.

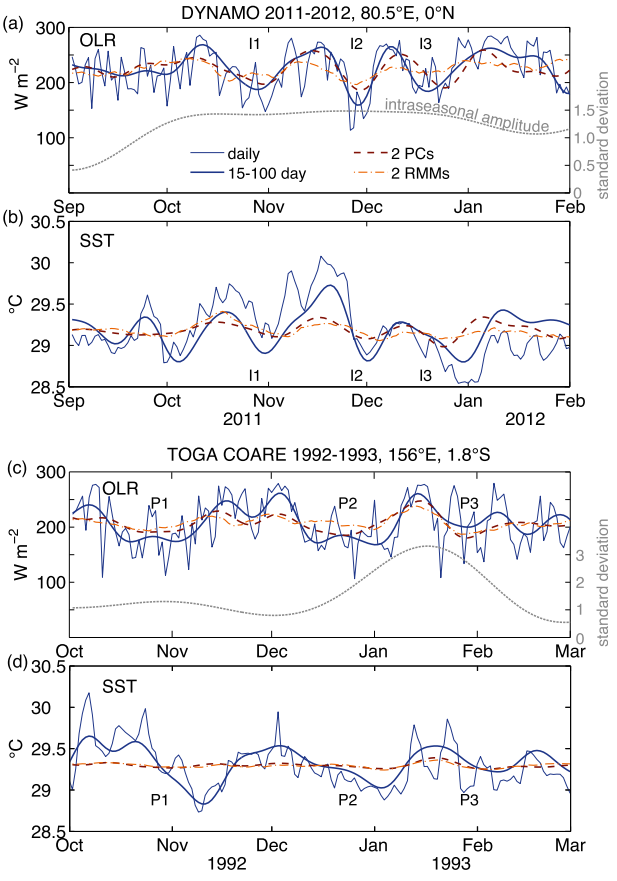

FIG. 4. (a),(c) OLR and (b),(d) SST at the locations of DYNAMO and TOGA COARE during their respective intensive observation periods. OLR and ERA-I SST anomalies regressed on the leading two intraseasonal OLR PC (red dashed) and the RMM (orange dotted–dashed) indices (Wheeler and Hendon 2004) underestimate the local daily (thin blue) and intraseasonal (thick blue) variability observed in TOGA COARE and DYNAMO. Labels I1, I2, I3, P1, P2, and P3 indicate times of low intraseasonally filtered OLR anomalies. The gray dashed line in (a) and (c) corresponds to the right axis and shows the 50-day low-pass-filtered normalized magnitude of the first two principal components of tropical intraseasonal OLR.

OLR was low over the western Pacific TOGA COARE experiment for two 10–20-day intervals, labeled P1 and P2 in Figs. 4c,d. A third period of modestly decreasing SST in TOGA COARE at the end of January 1993 (P3) has a weak minimum of intraseasonal OLR. The projections of the PCA and Real-Time Multivariate MJO (RMM; Wheeler and Hendon 2004) indices indicate that the canonical planetary intraseasonal structure associated with low OLR at 1.8°S, 156°E is present for P3. SST has weaker variability than OLR on shorter time scales. The NCEP SST used by ERA-I in 1992/93 is only weekly, so for a fairer comparison to the daily SST in DYNAMO, we use NOAA Optimally Interpolated version 2 daily SST (Reynolds et al. 2007) at the TOGA COARE location in Fig. 4d.

TABLE 2. Dates of minimum OLR and SST in intraseasonal events during DYNAMO and TOGA COARE.

Event	OLR min	SST min
DYNAMO		
I1	29 Oct 2011	31 Oct 2011
I2	28 Nov 2011	1 Dec 2011
I3	20 Dec 2011	30 Dec 2011
TOGA COARE		
P1	22 Oct 1992, 3 Nov 1992 centered on 28 Oct 1992	11 Nov 1992
P2	16 Dec 1992, 2 Jan 1993 centered on 24 Dec 1992	3 Jan 1993
P3	30 Jan 1993	7 Feb 1993

TABLE 3. Peak-to-trough range of daily and intraseasonally filtered OLR and SST in DYNAMO. Local regression of the first two PCs and RMM indices captures less of the observed daily variance. The percentage of the daily OLR peak-to-trough range retained by the filtering and regressions on global indices is shown in parentheses.

	ΔOLR ($W m^{-2}$)	ΔSST (°C)
Daily	160	1.0
15–100 day	110 (68%)	0.9
2 PCs	90 (56%)	0.3
2 RMMs	35 (21%)	0.2

Local time series show the local effects of daily and intraseasonal variability on OLR and SST (Fig. 4). The magnitude of the vector formed from the first two PCs is about 1.5 standard deviations for most of DYNAMO as shown by gray dashed line in Fig. 4. In TOGA COARE the magnitude of the PCs has one long enhancement with a maximum of 3.4 standard deviations in January 1993.

The two PCs efficiently representing the MJO on a global scale are correlated to the local intraseasonal variability, but their local peak-to-trough range in DYNAMO is only 56% of the range of the daily time series, and only 80% of the intraseasonally filtered OLR range (Table 3). The local peak-to-trough range indicates the strength of local extrema in late 2011, but is not representative of the amount of variance explained. The range of the RMM projection is only 30% of the local intraseasonal OLR peak-to-trough range. Regressions of the OLR PC or the RMM index underpredict the local SST range even more. Therefore, much of the observed intraseasonal variability in the DYNAMO and TOGA COARE observations is due to local or regional phenomena that are not closely linked to the global-scale development and propagation of the MJO.

b. *DYNAMO and TOGA COARE time series*

We next present time series from DYNAMO observations from the R/V *Roger Revelle* at the equator, 80.5°E (Fig. 5). The intraseasonal minima of OLR (I1, I2, and I3) are associated with negative net surface heat flux, clouds and rain, eastward wind stress, cooler air temperature, and decreasing SST. The timing of strong individual rain, stress, or heat flux events can differ by up to several days from the time the intraseasonal OLR reaches a minimum.

Figures 5 and 6 are modeled after Fig. 3 of Anderson et al. (1996). Figure 5a shows daily average solar, latent, sensible, and net heat fluxes. As over most of the tropical oceans, the net downwelling surface solar radiation was the only term of the surface fluxes that warms the ocean. Its mean exceeded 200 $W m^{-2}$ on most days, larger than the sum of sensible, latent, and net longwave radiative flux cooling the ocean. The average heat flux gained by the ocean at the surface during the three *Revelle* deployments to the equator was 43 $W m^{-2}$. Days with negative net heat flux (highlighted with pale green bars) corresponded to convective conditions.

Clouds extinguished the incoming solar radiation, usually to less than 100 $W m^{-2}$, for all of the days of negative net surface heat flux. The blue shaded area in Fig. 5b corresponds to hourly clear-sky fraction (the white area extending from the top of the axis corresponds to the cloud fraction). Less cloud fraction corresponds to more daily average solar radiation (Fig. 5a). Some of the clouds were dynamically vigorous enough to rain. Figure 5b shows the daily average rain rate averaged over the 1257-km^2 area within 20 km of the ship from the Colorado State University TOGA radar (Thompson et al. 2014, manuscript submitted to *J. Atmos. Sci.*) (gray bars in Fig. 5) and sampled by the PSD rain gauge on the ship (gray circles in Fig. 5a). The maximum daily rain sampled on the ship in the three legs was 7.5 mm h^{-1} on 28 October 2011. On these days there was reduced solar radiation and net surface cooling of the ocean surface. Because rain is notoriously unevenly distributed, the rain at the gauge on the ship was subject to considerable variability, yet the daily rain rate from the radar area corresponded well (r = 0.64) to the rain measured on the ship.

Most days with negative net surface heat flux also had stronger zonal wind stress. (The wind stress magnitude is correlated to the zonal wind stress magnitude at r = 0.98, and meridional wind stress is strongly correlated with zonal wind stress.) Mean zonal wind stress for the *Revelle* deployment on the equator in DYNAMO was 0.028 ± 0.005 N m^{-2} eastward (i.e., a mean westerly wind). Unlike westward stress under trade winds, which drives equatorial upwelling, the mean eastward wind stress drives Ekman convergence on the equator, resulting in equatorial downwelling. However, the zonal wind stress occurs

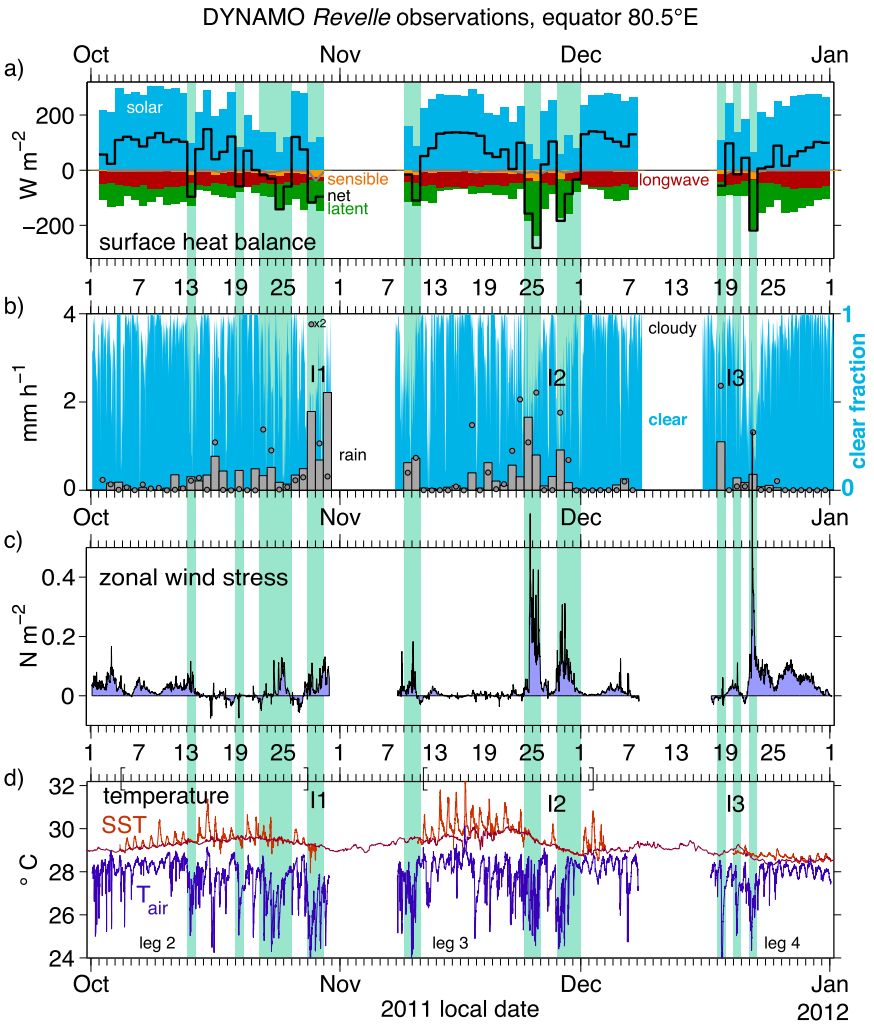

FIG. 5. (a) Daily average surface heat fluxes incident on the ocean (positive warms the ocean) in DYNAMO, averaged over each local solar day at the equator, 80.5°E. Solar radiation (blue) is compensated by evaporation (green), longwave radiation (red), and sensible heat flux (orange), resulting in the net surface heat balance (black). (b) Variations in cloud fraction (clear fraction indicated in blue) and rain from the TOGA precipitation radar averaged within 20 km of the ship (bars) and ship optical rain gauge (circles). (c) Hourly running mean of 10-min zonal wind stress. (d) The 10-min 0.1-m depth sea surface temperature (from the R/V *Roger Revelle* when stationed at 0°, 80.5°E, orange). Ocean temperature at 10-m depth from the OSU Ocean Mixing Group Chameleon profiler (dark red), and the UW/APL buoy (0°, 79°E) when the ship was off station. Surface air temperature (blue) measured on the ship in the DYNAMO experiment. Green shading behind all panels highlights days negative net surface heat flux cooled the ocean.

in short bursts that last several days. Stress observations exceeded 0.2 N m^{-2} for a total of 27 h (1.5% of the time sampled) during DYNAMO and the peak stress was 1 N m^{-2}. Such (eastward) westerly wind bursts can drive mixing of temperature and salinity across the thermocline (Smyth et al. 1996), and accelerate zonal currents in the ocean, whose convergence initiates downwelling waves in the equatorial thermocline that in the Pacific Ocean lead to equatorial El Niño–Southern Oscillation (ENSO) anomalies (McPhaden et al. 1992).

Intraseasonal cycles of SST were observed on *Revelle* during the months of October and November during DYNAMO. The ocean also responds thermodynamically to the surface heat flux. SST increased gradually in the beginning of October, November, and December, reaching maximum temperature at 0.1-m depth on the afternoons of 15 October and 16 November 2011, and probably during the *Revelle*'s port call and transit between legs 3 and 4 (Fig. 5d). The SST cooled in the periods with negative net heat flux. The 0.1-m SST shows

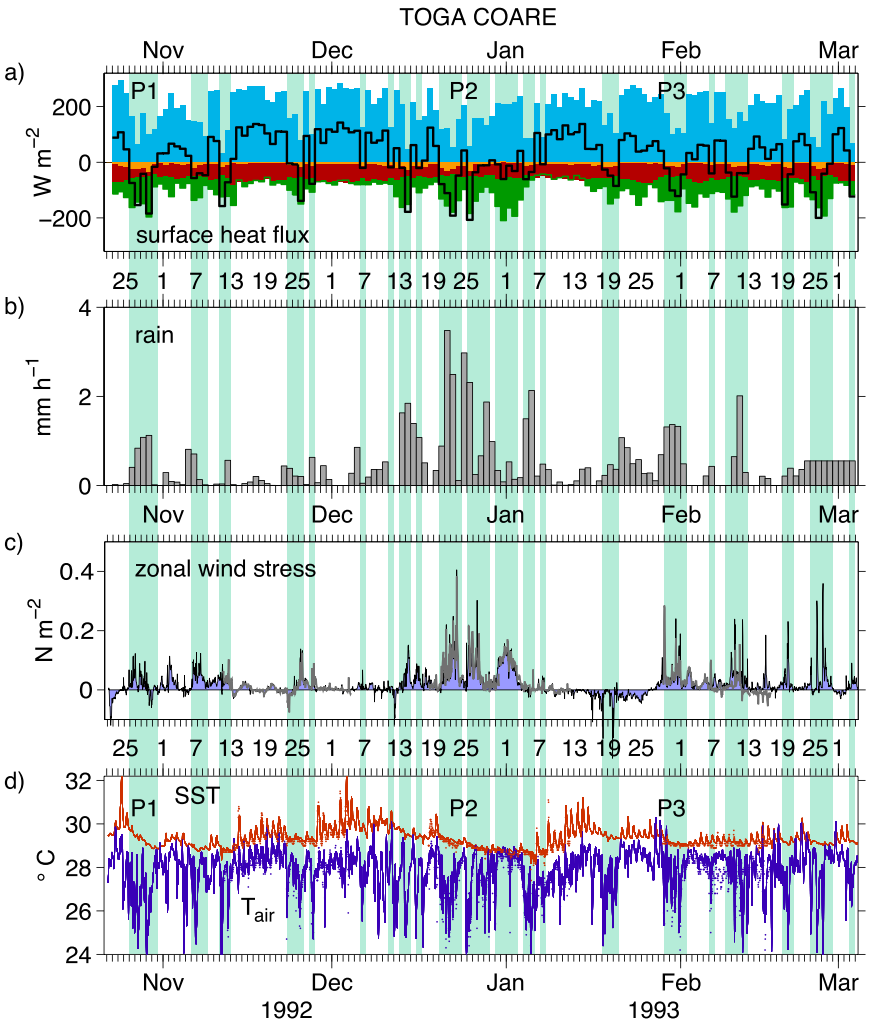

FIG. 6. As in Fig. 5, but for hourly data from the R/V *Moana Wave* and the IMET buoy in TOGA COARE. Wind stress (gray line *Moana Wave*, shaded IMET), SST (red line 0.45-m IMET, dots *Moana Wave*), and air temperature (blue line IMET, dots *Moana Wave*). [IMET data courtesy S. P. Anderson and R. Weller as in Anderson et al. (1996).]

strong diurnal warming during the periods of gradual SST warming, especially 5–22 October and 11–23 November. Ocean temperature at 10-m depth [taken from the Oregon State University (OSU) Chameleon profiler or the nearby University of Washington/Applied Physics Laboratory (UW/APL) buoy when the *Revelle* was off station] was usually slightly cooler and had a delayed and muted diurnal warming [consistent with the model of Price et al. (1986) and observations of Anderson et al. (1996)]. The warmest 10-m temperature occurred on 19 October (excepting a 2-h anomaly on 16 October) and 22 October, a few days later than the peak temperature at 0.1 m. The 0.1-m ocean temperature was usually as warm as or warmer than the 10-m temperature, but there were brief exceptions. These times were probably associated with rain deposited at the wet bulb temperature, which is colder than the air temperature. During calm periods rain also freshened and stratified the upper few meters of the ocean briefly, trapping the cooling of the surface heat fluxes within a shallow layer (this shallow layer is still warmer than the atmosphere) without changing the vertical profile of absorption of solar radiation.

Some days show no diurnal cycles of SST. On these days the temperature decreased at 0.1- and 10-m depth alike (Fig. 5d). One or two days with no diurnal cycle of SST were found in the intraseasonal slowly warming phase (13 and 19 October), but most of the days with no diurnal SST layer were in the cooling phase of the intraseasonal oscillation. Notably on 24–25 and 28–29 October and on 24–25 and 28–30 November there was no diurnal warming. These days also had negative daily average net surface heat (and buoyancy) flux and strong wind stress

TABLE 4. All-experiment mean (±standard error) of daily heat fluxes (here E denotes latent heat flux, H sensible heat flux, LW longwave radiative flux, and SW shortwave radiative flux) and precipitation P sampled by the IMET buoy dataset (Anderson et al. 1996), by the R/V *Moana Wave* in TOGA COARE, and by the R/V *Roger Revelle* in DYNAMO. The number of degrees of freedom (n_{dof}) equals the number of days for DYNAMO, but for TOGA COARE is the number of days divided by 1.5 due to the slight autocorrelation of the TOGA COARE daily time series.

DYNAMO vs TOGA COARE experiment mean surface fluxes ($W m^{-2}$)					
	n_{dof}	Net	$E + H + LW$	SW	P
TOGA COARE (1992/93)					
IMET	88	18 ± 7	−176 ± 3	193 ± 3	324 ± 46
IMET (*Moana Wave* sampling)	34	23 ± 12	−171 ± 6	194 ± 9	341 ± 83
R/V *Moana Wave*	34	29 ± 13	−168 ± 6	197 ± 10	276 ± 80
DYNAMO (2011/12)					
R/V *Roger Revelle*	75	43 ± 11	−173 ± 4	216 ± 9	210 ± 34

that quickly distributed solar heating throughout the upper ocean mixed layer. The surface temperature without diurnal warming occurred atop two periods that the 10-m temperature decreases on a longer time scale. In the convective period I1 the 10-m depth ocean temperature decreased −0.7°C during 22–30 October, and in period I2 the temperature decreased −1.3°C during 22 November–1 December. Ocean temperature also varies because of nonlocally forced advection. Some temperature changes at 10 m (Fig. 5, dark red) were coherent with changes below the mixed layer (e.g., 16–19 November) and unrelated to local surface stress, heat flux, or the solar cycle (K. Pujiana 2014, personal communication).

All DYNAMO convective events had eastward wind stress and cooled the ocean by net upward surface heat flux, but each event had a unique progression of features. Event I1 had the strongest precipitation at the ship. Event I2 had two distinct bursts of eastward wind stress, each one associated with a burst of convection (Moum et al. 2014). Intraseasonal event I2 had two maxima of rain at the ship and two minima in daily OLR. According to time–longitude plots from satellite retrievals of OLR and rain, these features of deep atmospheric convection propagated eastward over the *Revelle* at 8–9 $m s^{-1}$ [Yoneyama et al. (2013); Moum et al. (2014), their Fig. 3], the phase velocity expected for a convectively coupled Kelvin wave (Kiladis et al. 2009). The *Revelle* observed only the conclusion of convection from event I3. This was then followed by the strongest wind stress observed in DYNAMO and a week-long period of enhanced eastward wind stress without convective activity.

Air temperature measured on the ship (adjusted by flux-gradient similarity to 10-m height; blue, Fig. 5d) was considerably more variable than ocean temperature. Air temperature roughly followed SST during weeks of warming in the convectively suppressed periods early in each of the months of October, November, and perhaps December, with the air about 1°C cooler than the SST. The air–sea temperature difference was even more negative in the convective periods in late October and November. The air temperature dropped in brief episodic cold pools that can be identified by the air temperature dropping below 27°C. These cold pools were asymmetric in time, with sudden cooling followed by a gradual recovery of the temperature. Often the temperature dropped because of a second or multiple cold pools before recovering from an earlier cold pool. Cold pools varied in strength and recovery time. There were more and stronger cold pools during the convectively active phase of intraseasonal variability. Cold pools increased surface sensible and latent heat fluxes (Yokoi et al. 2014; Feng et al. 2014, manuscript submitted to *J. Adv. Model. Earth Syst.*).

The role of the surface fluxes and westerly wind bursts during the TOGA COARE (October 1992–March 1993) experiment on the upper western Pacific Ocean has been well documented. The 134-day time series from TOGA COARE IMET (1.8°S, 156°E; Weller and Anderson 1996; Anderson et al. 1996) and the R/V *Moana Wave* (1.7°S, 156°E for 11 November–3 December 1992, 17 December 1992–11 January 1993, and 28 January–16 February 1993; Fairall et al. 1996b) observations are shown in Fig. 6. Table 4 shows the mean net heat flux, the sum of the cooling, and the solar warming, as well as the standard error of their mean for DYNAMO and TOGA COARE. The mean net surface flux warming in TOGA COARE was only about 20 $W m^{-2}$, half the net surface warming observed in the central Indian Ocean in DYNAMO. This was mostly due to stronger solar radiation in DYNAMO (216 ± 9 $W m^{-2}$) than in TOGA COARE (193 ± 3 $W m^{-2}$). The average sum of latent, sensible, and longwave cooling is statistically indistinguishable between DYNAMO and TOGA COARE. The standard error of the mean net heat flux is larger than its constituents because daily solar and evaporation anomalies are of the same sign, even though their means have opposite signs.

The intraseasonal convectively active events P1, P2, and P3 (defined by OLR minima) in the western Pacific Ocean during TOGA COARE are indicated in Figs. 6a,d. They

coincided with groups of days with negative net heat fluxes, some that reach –200 W m^{-2}. As in DYNAMO, the diurnal cycle of SST was small during periods of enhanced wind stress and negative net heat flux, and large when the wind was calm (e.g., on 13–22 November 1992, 28 November–6 December 1992, and 8–16 January 1993).

Event P2 stands out as an example of strong rainfall, eastward wind stress, and evaporation. SST decreased for 24 days in the middle of TOGA COARE (12 December 1992–5 January 1993). Daily minimum SST at 0.45 m decreased by 1.5°C in P2. Zonal wind blew eastward in four consecutive 5-day bursts separated by wind stress minima. The first three were associated with convection. Daily average rain was greater than 1 mm h^{-1} for the first three of these bursts. The final strong wind burst blew during a minimum of rainfall. From 26 December to 3 January strong solar radiation and evaporation due to the wind canceled, finishing the long intraseasonal event P2 with small net heat fluxes weaker than 50 W m^{-2}. This event was unusual in its strength and duration. Yet the continuation of the eastward wind, which began during the time of convection and negative net heat flux, into the sunny and weak net heat flux conditions following the convection, was typical of events in TOGA COARE. Events P1 and P3 were followed by weak eastward wind stress and weak positive heat flux during 31 October–6 November 1992 and 2–9 February 1993, respectively. In DYNAMO, only convective event I3 was followed by strong wind stress after the convection cleared. SST at the end of TOGA COARE was nearly constant over four quasi-7-day synoptic vacillations between positive and negative net heat flux following P3. These vacillations were apparently driven by bursts of eastward wind stress on time scales shorter than the MJO, resulting in nearly simultaneous changes in the shortwave radiation and evaporation. We cannot confidently identify systematic differences between intraseasonal events in the Indian Ocean and western Pacific Ocean from the three diverse events sampled in each basin.

Synoptic convective events were found inside and outside of the convective envelope of the MJO in DYNAMO and TOGA COARE. For example, the 8–9 m s^{-1} eastward propagation of the two convective features in event I2 in DYNAMO suggests they were convectively coupled atmospheric Kelvin waves. Sounding anomalies on a 10-m vertical grid are computed by removing the vertical 11-point moving average of all DYNAMO–*Revelle* soundings (Fig. 7). As in Straub and Kiladis (2003, their Fig. 5), time progresses from right to left in Fig. 7 to emulate the zonal structure of the waves as they propagate eastward over the *Revelle*. The time-vertical structure of temperature, humidity, and zonal wind from rawinsondes released from *Revelle* in the two propagating wave features further resemble composites of Kelvin waves over Majuro (7°N, 171°E; Straub and Kiladis 2003; Kiladis et al. 2009) in several respects. First, upper-tropospheric temperature anomalies last about 2 days for each convective burst of event I2. Second, strong upper-tropospheric heating begins about a day before the maximum tropospheric warm anomaly at 200 hPa (Fig. 7, top). Third, specific humidity anomalies at 800–400 hPa lag the potential temperature anomaly by about 1 day. Zonal wind lags by an additional day and tilts westward with height. The eastward wind starts abruptly and appears to coincide with the end of the highest specific humidity anomalies. The propagation and vertical structure of the Kelvin waves were distinctly identified within the longer convective envelope of the MJO.

c. Daily atmospheric moisture budget

Some theories of the MJO depend sensitively on the distribution and feedback of moisture sources to the atmospheric column. We investigate whether the evaporation observed in DYNAMO and TOGA COARE is significantly correlated to the precipitation, and whether anomalous intraseasonal evaporation is a significant source of moisture to balance the observed precipitation. We find weak but statistically significant correlations of evaporation to precipitation (0.27 in TOGA COARE and 0.35 in DYNAMO, Fig. 8). The daily precipitation has a standard deviation of 290 W m^{-2} in latent heat units, much more than the 34 W m^{-2} standard deviation of evaporation. In situ observations show surface evaporation anomalies in the tropical warm pool positively contribute to the MJO precipitation, but it has a magnitude insufficient for generating and sustaining the precipitation associated with the MJO. Even if they were highly correlated, the evaporation anomalies would explain only about 10% of the variability of the precipitation.

The remaining >90% of the moisture must be supplied to precipitation by another source. The budget for the integrated water in the atmospheric column is

$$0 = \underbrace{-\frac{\partial}{\partial t}\frac{1}{g}\int_0^{p_s} q_{\mathrm{tot}}\, dp}_{\text{storage}} \underbrace{-\ \nabla\cdot\mathbf{F}_q}_{\text{convergence}} \underbrace{+\ E}_{\text{evaporation}} \underbrace{-\ P}_{\text{precipitation}}. \tag{1}$$

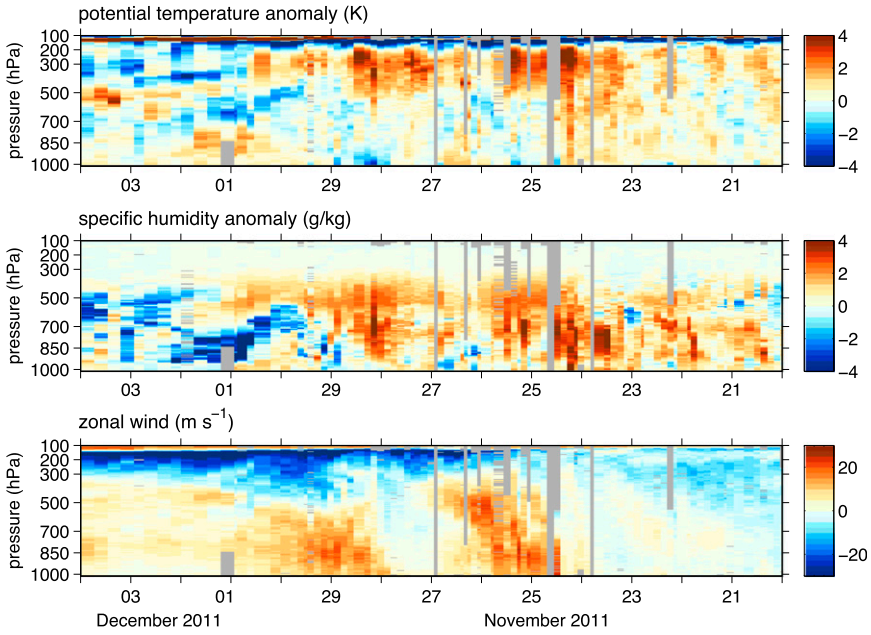

FIG. 7. Vertical structure of two convectively coupled Kelvin waves that passed over R/V *Roger Revelle* on 24–25 and 27–28 November. Time increases from right to left to demonstrate the zonal structure of the anomalies as they propagate from west to east. Gray areas indicate missing data.

The first term is the column moisture storage. The budget is written so that all four terms sum to zero, so negative storage means the column-integrated water is increasing. Moisture enters the column through vertically integrated horizontal moisture flux convergence and surface evaporation, and leaves by precipitation. The intraseasonal variation of our moisture flux convergence computed as a residual from the moisture budget over the ship agrees with the column-integrated moisture flux convergence from the northern sounding array (Johnson et al. 2014). Estimates from the TOGA COARE and DYNAMO radiosonde arrays indicate that most of the precipitating water is supplied by moisture flux convergence (Lin and Johnson 1996; Johnson and Ciesielski 2013).

We independently retrieve the column-integrated water using the microwave radiometer on the *Revelle* (Fig. 9a). From the integrated column moisture we estimate the storage, and then the convergence as a residual (Fig. 9b). The column-integrated moisture was variable from day to day, but systematically reached a maximum in each of the convective phases of the MJO. The intraseasonal range of integrated moisture during DYNAMO was about 2–3 cm, on a background of 5–6 cm. The anomalous storage of 2–3 cm would be consumed in about a day by a rain rate of 1 mm h^{-1}. Most daily rain rates were much less than 1 mm h^{-1}, yet 4 days of very strong rain (28 October, 30 October, 24 November, and 18 December 2011) exceeded 1 mm h^{-1} in the daily average, and 13 days (18% of the 71 local days sampled by the radar) exceeded 0.5 mm h^{-1}.

Daily precipitation in convective events easily exceeded the column supply of water, so the storage of water vapor seems to play a relatively passive role compared to other terms in the column water budget. During 11–26 October, when the water vapor increased prior to convective maximum I1, the storage was variable but averaged $-20\,W\,m^{-2}$, compared to convergence of $140\,W\,m^{-2}$, evaporation of $100\,W\,m^{-2}$, and rain of $210\,W\,m^{-2}$. The column-integrated water vapor sometimes took on larger values, therefore, its intraseasonal variation was not limited by being close to saturation.

Moisture flux convergence was usually on the order of the precipitation. It weakly exported moisture from the column between convective events (5–9 October, 12–18 November, and 25–29 December). Moisture flux convergence imported moisture, approximately balancing intermittent showers, in the several days before the convective maxima. This is in contrast to the beginning of the convective maxima, when moisture flux convergence of 1500–3000 $W\,m^{-2}$ was balanced by rain and increases in column moisture storage. Total column water increased despite the strong rain.

On 28 November there was positive storage (depletion of water) in the second Kelvin wave of I2. We cannot sample all the terms in the budget over the complete convective lifetimes of events I1 and I3, but

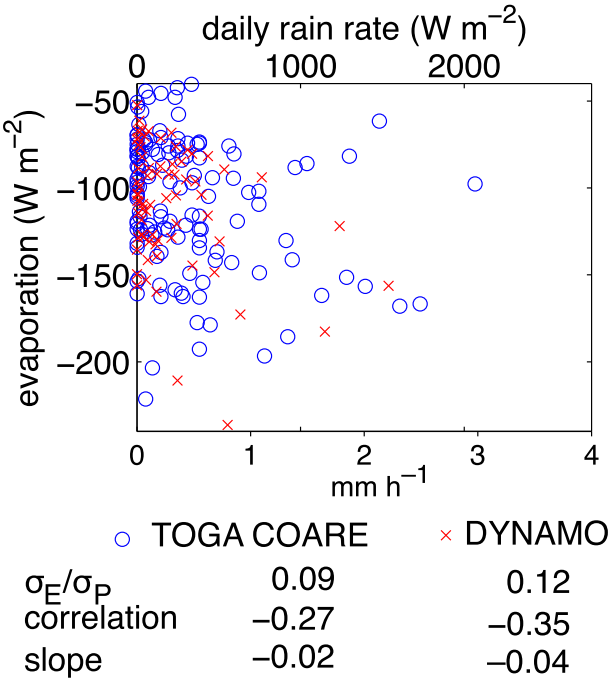

FIG. 8. Evaporation vs daily averaged rain rate averaged over several stations from TOGA COARE (blue circles) and over the 20-km radius radar disk around the R/V *Roger Revelle* in DYNAMO (red crosses).

storage became positive later in I1 on 30 October, and was positive at the end of I3 (beginning of leg 4) on 19 December, suggesting column water anomalies decreased toward the end of intraseasonal convective events. With a mean and standard deviation of 110 ± 30 W m^{-2}, evaporation is moderate and very constant compared to fluctuations in rain (210 ± 290 W m^{-2}), storage (zero in the mean, but −30 ± 300 W m^{-2} over the three *Revelle* legs), and moisture flux convergence (110 ± 460 W m^{-2}).

d. Intraseasonal air–sea interaction composites

The DYNAMO and TOGA COARE experiments each were able to sample several intraseasonal convective events. Now we place the events observed in DYNAMO and TOGA COARE in the context of typical intraseasonal events from global datasets. A composite average of a large number of events retains systematic intraseasonal variability, and removes random variability that only affects individual events. Global datasets also show the zonal-time evolution of intraseasonal convective events from the Indian Ocean to the Pacific Ocean, including the DYNAMO and the TOGA COARE locations. The gridded data extend the temporal and spatial sampling beyond the experiments, and allow comparison between station observations of MJO structure to larger reanalysis-based MJO structures. The analysis determines whether there are robust differences between intraseasonal variability observed in the central Indian Ocean compared to the western Pacific Ocean.

Based on the principal component analysis, 103 intraseasonal events satisfied a criterion of strong amplitude and eastward propagation (appendix B). We composite the full unfiltered anomalies of TropFlux gridded analysis surface flux variables during these events on the phase of the MJO described by the leading two modes of principal component analysis of OLR. Figure 10 shows the composite of the 103 events. The cycle before and the cycle after the center of the event, when the MJO attains a convective maximum near 80°E, are each divided into 24 phase bins. Daily data within ±60 days of the center of the event are composited according to their intraseasonal phase. The compositing procedure is described further in appendix B. Black contours in each panel show the negative OLR anomaly of the first two principal components.

Color-shaded contours show the 103-event composite of OLR, SST, and surface fluxes. The two PCs explain 37% of the intraseasonal OLR variance, so the composite OLR (Fig. 10a) recovers nearly the same pattern as the first two PCs of OLR used to construct the composite. The minimum unfiltered OLR composite (shaded) slightly leads the PC–OLR regression (contoured, Fig. 10a). Convective events rapidly develop their minimum OLR with a quick onset, and then slowly recover. Intraseasonal filtering and regression slows the apparent onset and shifts the minimum OLR later relative to the unfiltered composite. The composite SST and surface fluxes also have alternating eastward-propagating anomalies. Sea surface temperature and SST tendency (Figs. 10b and 10c) show SST cooling during the convective phase of the events, which is consistent with the cooling by the net surface heat flux during the convective phase of the MJO.

The amplitude and relative phase relation among the OLR, wind stress, SST, and each of the components of the surface heat flux is relatively consistent across the warm pool from the central Indian Ocean to the western Pacific Ocean. The net surface heat flux is synchronous with OLR anomalies. Each of the components of the net surface heat flux is phased slightly differently, yet the relative phase among the components is consistent throughout the warm pool. The largest surface heat flux term, and that with the greatest intraseasonal composite amplitude (25 W m^{-2}) is the solar radiation absorbed by the ocean in phase with high OLR. (The surface solar radiation in gridded datasets is not independent of OLR. ISCCP uses OLR retrievals to constrain the surface radiation, and after 2007 TropFlux surface solar radiation

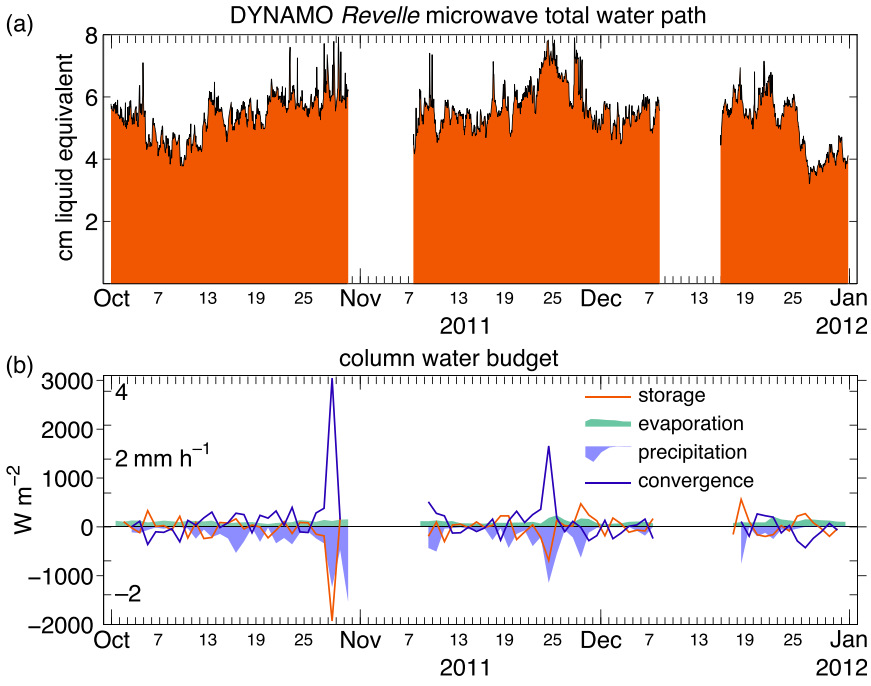

FIG. 9. (a) Hourly total water path (centimeters liquid water equivalent, or $10^5\,\mathrm{kg\,m^{-2}}$) retrieved by microwave radiometer from the R/V *Roger Revelle*. (b) Daily column-integrated water budget: precipitation from radar within 20-km range of the ship, evaporation from bulk flux algorithm, storage from microwave radiometer, and moisture convergence from the residual.

is parameterized as a regression on OLR.) Some $3\,\mathrm{W\,m^{-2}}$ of the solar radiation is offset by longwave radiation anomalies, though the longwave anomalies lead the OLR by less than a quarter phase, perhaps indicating warm moist anomalies and emissive clouds in the lower troposphere before the intraseasonal maximum of deep convective clouds.

Eastward wind stress is nearly synchronous with the OLR anomalies, so strong zonal convergence accompanies the front (eastern) edge of the convective anomalies from 70°E to the date line. Sensible heat flux ($\pm 2\,\mathrm{W\,m^{-2}}$, 25% of its mean) out of the ocean slightly leads, while latent heat flux ($\pm 10\,\mathrm{W\,m^{-2}}$, 10% of its mean) slightly follows the low OLR anomaly. The phase of the surface heat fluxes can be explained by their factors: the friction velocity scale $u^* = (|\tau|/\rho)^{1/2}$ (where τ is the wind stress and ρ is air density) and turbulent temperature scale T^* for sensible heat flux, or turbulent humidity scale q^* for latent heat flux. Figure 11 shows the eastward wind stress (and, hence, u^*) maximum slightly follows the peak of convection. Anticorrelation of intraseasonal q^* with wind stress anomalies weakens the intraseasonal amplitude of the latent heat flux. Surface air temperature is cooled by convection, enhancing sensible heat flux at the leading edge of the convective anomaly.

The anomalies of OLR, SST, and surface heat fluxes become weaker over the Pacific Ocean east of 170°E where climatological SST decreases below 29°C (Fig. 11). Zonal wind anomalies remain strong, however. The mean background wind reverses sign around 155°E (Fig. 2b) changing the configuration of intraseasonal surface heat flux anomalies relative to wind stress over the eastern Pacific Ocean. The phase velocity increases considerably as the convective MJO transitions to a dry Kelvin wave.

5. Discussion

Gridded flux products based on reanalyses (OAFlux and TropFlux) agree well with DYNAMO observations from the R/V *Roger Revelle* at 0°, 80.5°E, and with TOGA COARE observations from the R/V *Moana Wave* at 1.7°S, 156°E. The NCEP–DOE reanalysis and ERA-I both ingest data from RAMA/TAO buoys. The nearest RAMA buoy is within 5 km of the *Roger Revelle* station in DYNAMO, and the TAO buoy at 2°S, 156°E is within 50 km of the *Moana Wave*, which may have improved the performance of the reanalysis-based surface flux products there, compared to locations far from any observations.

The evolution of intraseasonal convective and air–sea interaction anomalies (SST and surface fluxes) was

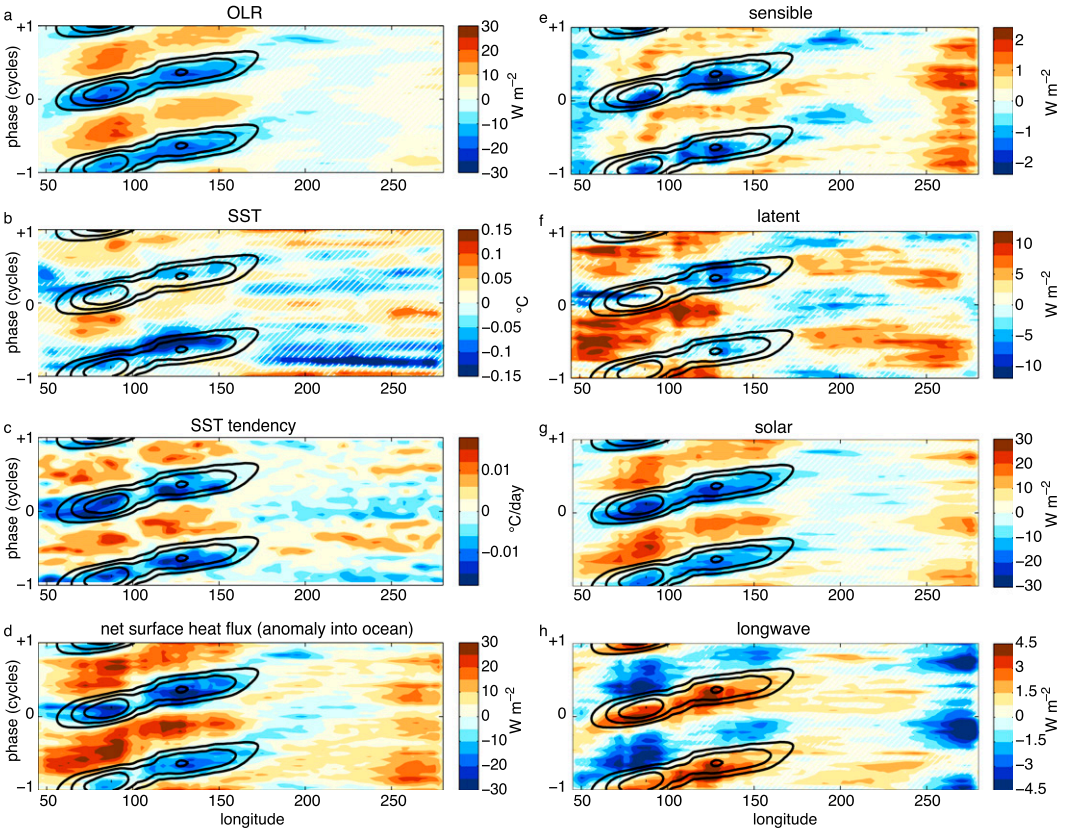

FIG. 10. Longitude–phase plots of (a) OLR, (b) SST, (c) SST tendency, and (d)–(h) heat flux anomalies for 103 strongly eastward-propagating convective events composited by intraseasonal phase before and after their OLR is minimum at 80°E. Positive fluxes warm the ocean. The black contours in each panel show the low-OLR anomaly of the convective phase of the MJO constructed from the first two leading EOFs. White hatching covers SST and component flux anomalies that are not statistically significant at 95% confidence (except SST tendency is significant only at its peaks, and net surface heat flux is significant almost everywhere). As in Figs. 5 and 6, negative surface heat fluxes cool the ocean.

observed for three convectively active MJO events in the central Indian Ocean in DYNAMO (2011/12) and three MJO events in the western Pacific Ocean warm pool in TOGA COARE (1992/93). The results of the experiments showed slightly larger variations in evaporation averaged over TOGA COARE ($40\,W\,m^{-2}$) compared to DYNAMO ($30\,W\,m^{-2}$). The SST (29.1° ± 0.5°C versus 29.2° ± 0.4°C) and latent heat fluxes (both $110\,W\,m^{-2}$) were indistinguishable between the two experiments. The stronger latent heat flux variability in TOGA COARE could be due to the growth of MJO anomalies as they propagate eastward, larger ocean heat capacity in the western Pacific, or it could be due simply to sampling different local realizations of six unique individual events.

Are these two handfuls of intensely observed MJO realizations representative of a typical MJO? The composite of 103 MJO event anomalies in Fig. 10 grows in amplitude in the central Indian Ocean, reaching its maximum amplitude around 80°E, which corresponds to the location of the DYNAMO field campaign. The MJO maintains nearly constant amplitude, with a slight dip over the Maritime Continent, until it reaches about 160°E. The intraseasonal composite OLR amplitude is slightly weaker over 155°E than over 80°E. The stronger events observed during TOGA COARE were stronger for their own individual reasons, rather than a systematic longitude dependence of typical MJO events. The 103 convective events in the composite were chosen for their persistent amplitude and eastward propagation. It is possible that some less persistent intraseasonal convective events do not propagate eastward significantly, but have strong local signatures over the central Indian Ocean or western Pacific Ocean.

Air–sea interaction observed in DYNAMO and TOGA COARE results from a variety of atmospheric (and oceanic) waves embedded within the intraseasonal variability. There is considerable synoptic atmospheric

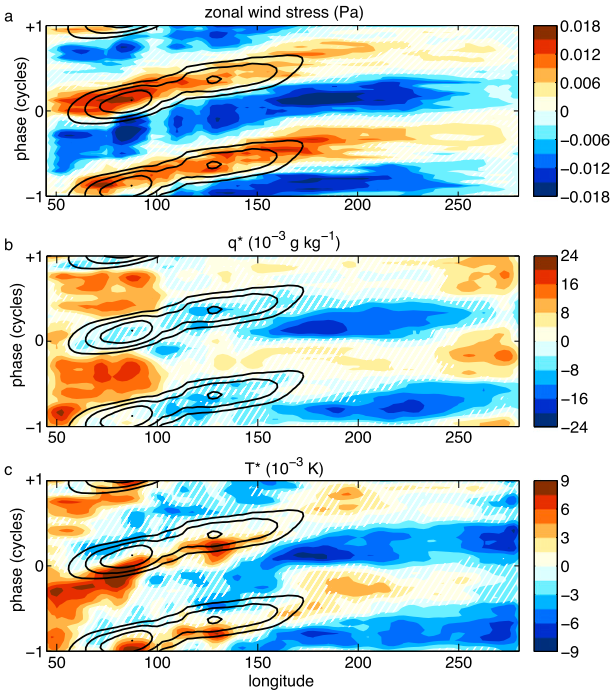

FIG. 11. (a) MJO composite zonal surface wind stress, (b) turbulence specific humidity scale q^*, and (c) turbulence temperature scale T^* over the Indian and Pacific Oceans, as in Fig. 10.

variability in the DYNAMO and TOGA COARE station time series. Some of the convective disturbances observed in the TOGA COARE and DYNAMO field experiments were related to the MJO, and others were not. The onset of two convectively coupled Kelvin waves passing over the ship within the intraseasonal convective maximum I2 in late November 2011 is an important and well-observed example of oceanic and atmospheric processes within the MJO (Moum et al. 2014). On the other hand, the strong synoptic variability in the wind stress, rain, and fluxes observed in TOGA COARE in February 1993 project little onto intraseasonal time scales.

East of 80°E, zonal wind stress is steady and easterly for most of the suppressed phase and for the beginning of the convective onset as composite OLR anomalies become more negative than $-5\,\mathrm{W\,m^{-2}}$. Wind stress rapidly becomes eastward, reaching its maximum approximately 1/16 of a period after the time of minimum OLR. The wind stress relaxes gradually following the maximum and flattens out in the suppressed phase. Hendon and Glick (1997) show the eastward wind burst and evaporation maximum lagging the convection by approximately 1 week (more than 1/8 phase) behind the convection in the warm pool. The difference between their result and ours could be explained by our compositing of the unfiltered anomalies on the phase of the intraseasonal anomaly, compared to their time-lagged regression against a narrower (30–90 day) band of intraseasonal OLR (e.g., their Fig. 11). Spectral truncation of the sharp rise and slow relaxation of the wind in our composite will shift the eastward wind maximum later.

Lag regressions in the Indian Ocean (Hendon and Glick 1997; Woolnough et al. 2000) show the timing of the wind stress even later and farther westward of the surface convection. In DYNAMO wind stress rose sharply to a maximum within a few days of the maximum convection. The nearly synchronous phase relation of wind stress and fluxes with convection agrees with the phase relations found by Zhang and McPhaden (2000, their section 3c) from their analysis of TAO buoy observations in the tropical western Pacific warm pool. The phase of the zonal wind stress, heat flux, and SST to OLR is constant from 80° to 160°E in our composite intraseasonal event.

Few research cruises venture to the poorly observed waters west of 70°E longitude because of the danger of piracy. According to the reanalysis-based flux composites, the phase relation of the zonal wind stress, net heat flux, and SST is different at 40°–70°E longitude, and it is over this region that MJO OLR anomalies grow. Here eastward wind stress, surface heat flux, and cool SST develop uniformly with longitude across 50°–80°E after a negative OLR anomaly has propagated eastward and intensified to a maximum at 70°E (Fig. 11). The zonally uniform wind stress west of 70°E then propagates with OLR from 80° to 160°E. In the western Indian Ocean SST responds more strongly to intraseasonal surface fluxes than the central and eastern Indian Ocean. Its response to the net surface heat flux is twice as large at 50°E as it is east of 80°E.

The eastward wind stress in the western Indian Ocean is consistent with frictional flow toward low surface pressure induced under the convective heating anomaly growing to the east. The cool SST anomaly in the western Indian Ocean reinforces the pressure gradient pushing the eastward wind anomaly. The phase of the wind anomaly at 50°E is consistent with the convergence in Hendon and Salby (1994, their Fig. 8c) and the latent heat flux in Hendon and Glick (1997). The timing of wind stress to convection in the central Indian Ocean is the same as farther east, yet it is possible that the climatological western Indian Ocean SST gradient and the long fetch of eastward wind stress collects moisture evaporated over a large area extending approximately 2000 km to the west, and thereby amplifies convective anomalies in the central Indian Ocean.

Surface evaporation is the process through which most of the solar energy absorbed by the ocean enters the atmosphere. In moisture mode quasi-equilibrium

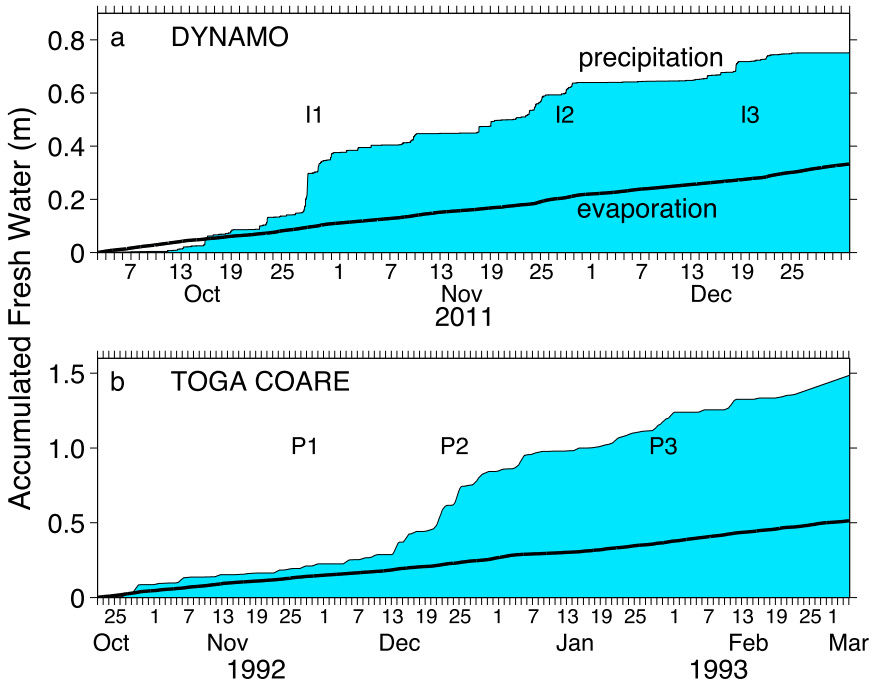

FIG. 12. Accumulated precipitation (from in situ ship, IMET, and TAO/RAMA buoys) and evaporation from the (a) DYNAMO and (b) TOGA COARE experiments.

theories of the MJO, evaporation anomalies are proposed as a means of increasing the column moist static energy in the convective region in order to grow the convective anomaly (e.g., Maloney and Sobel 2004; Sugiyama 2009). In TOGA COARE (Lin and Johnson 1996) and DYNAMO (Figs. 9 and 12) observations, local mean evaporation is less than ½ of the mean precipitation. Evaporation is moderate and steady compared to fluctuations of the precipitation and horizontal moisture flux convergence. Daily average evaporation increases 40% in westerly wind bursts, while daily precipitation maxima are an order of magnitude greater. Evaporation moistens the boundary layer slowly, so boundary layer moisture convergence must fetch moisture from a large area to explain the maxima in precipitation. We refer to "moisture fetch" as both the large area of the atmospheric boundary layer moistened by surface evaporation, and the process by which the large-scale circulation fetches moisture over this large area to feed the convection. The challenge for MJO theories then is to explain by what process relatively uniform evaporation and boundary layer moisture converges into the region of convection.

Maloney (2009) found advection of moisture and surface evaporation contributed in similar magnitude to lower-tropospheric moist static energy anomalies, but evaporation opposes the recharge of moist static energy in the suppressed phase. While SST anomalies have only a small effect on the fluxes, it is possible that positive SST anomalies over a large area in advance and east of convection can induce a broad area of low surface pressure and large-scale frictional convergence (e.g., Lindzen and Nigam 1987; Back and Bretherton 2009). This boundary layer convergence would fetch moisture from a wide area of the planetary boundary layer, having average surface evaporation, toward convectively coupled precipitating atmospheric waves. DeMott et al. (2014) described enhancement of the MJO by systematic moisture convergence over warm SST east of the convection in atmosphere–ocean coupled general circulation models.

Frictional boundary layer convergence on the equator east of the convective maximum has been found to destabilize the atmosphere to convection (Rui and Wang 1990; Maloney and Hartmann 1998). Maloney and Kiehl (2002) observed that intraseasonal SST anomalies in the eastern tropical Pacific Ocean also induced surface convergence. The result of a quasi-equilibrium model would be enlightening were it to explicitly include boundary layer convergence resulting from intraseasonal SST anomalies. The boundary layer adjustment to SST anomalies is a potential source of instability for intraseasonal convective anomalies, even if there are only weak temperature gradients in the free troposphere. The role of nonlinear moisture advection was key to eastward-propagating anomalies in the Sobel and

Maloney (2012) quasi-equilibrium model. The effect of intraseasonal SST anomalies on it could also be assessed.

6. Conclusions

DYNAMO, TOGA COARE, and gridded flux analysis composites have wind stress, convergence, and heat fluxes nearly in phase with convection from 70° to 160°E, consistent with previous findings from in situ observations in the warm pool (Zhang and McPhaden 2000). Eastward wind stress increases rapidly in the convective phase as wind converges slightly before (east of) the minimum OLR anomaly. Net heat flux anomalies are nearly in phase with the convection indicated by low OLR, with sensible heat flux strongest at the onset of convection, and wind stress and latent heat flux increasing as the convective phase matures. Convection, wind stress, and other related variables have a rapid onset followed by a slow recovery. Intraseasonal filtering of these variables' asymmetrical temporal structure introduces phase delays.

In TOGA COARE, DYNAMO, and the gridded flux products, net surface fluxes out of the ocean increase during the convective phase of the MJO, mostly from enhanced evaporation due to stronger wind and decreased solar radiation due to clouds. Surface turbulent fluxes are relatively steady over intraseasonal time scales, with composite cycles in gridded flux analyses with ranges of only $\pm 2\,\mathrm{W\,m^{-2}}$ (25%) for sensible heat flux and $\pm 10\,\mathrm{W\,m^{-2}}$ (9%) for latent heat flux (Fig. 10). Daily flux anomalies 3 times larger than the gridded analyses were observed in DYNAMO, roughly consistent with the larger daily OLR and SST anomalies than their intraseasonal regression time series (Fig. 4).

The observations help us assess the contribution to the MJO of three conceptual models of atmosphere–ocean interaction: surface flux feedback, coupled ocean–atmosphere interaction, and atmospheric moisture recharge. The phase of surface fluxes to the MJO convective anomaly suggests that intraseasonal surface fluxes increase moist static energy during MJO convection, contributing a positive feedback. The surface evaporation increases 30%–50% relative to its mean during the convective phase, yet this anomaly constitutes less than 10% of the moisture required for the precipitation (Fig. 12). The magnitude of the anomalous surface flux is only a small contributor to the moisture (or moist static energy) budget, but moisture mode theories do not require significant local evaporation anomalies for precipitation. For strongly negative gross moist stability only a small amount of evaporation is needed to destabilize the column to generate precipitation and moisture convergence. In these models evaporation does not drive precipitation directly through recharging the available water budget, but by destabilizing and increasing the moist static energy of the column that then induces large-scale moisture flux convergence.

Intraseasonal SST anomalies suggest that coupled ocean–atmosphere variability also amplifies the MJO. The SST and ocean mixed layer temperature responds to the intraseasonal variability of the fluxes. SST increases during the suppressed phase, reaching a maximum at the onset of convection. Mixed layer ocean temperature (measured at night or at 10-m depth) has an intraseasonal range of 1°–2°C in TOGA COARE and DYNAMO. The intraseasonal composite SST has a range of only about 0.2°–0.3°C, similar to Hendon and Glick (1997, their Fig. 11), Zhang and McPhaden (2000, their Fig. 11), and Benedict and Randall (2007, their Fig. 4c). We cannot completely explain this striking difference between SST time series from the field experiments and the analyses. The ocean temperature's response to the MJO events observed in TOGA COARE and DYNAMO appear to have been stronger than average.

Most satellite SST products avoid sampling during the day, so the effect of the diurnal warm layer is nearly absent from the gridded products. Calm wind and strong solar flux raise the SST in the suppressed intraseasonal phase, as measured at 0.1 m in DYNAMO and TOGA COARE (Marion 2014). Diurnal SST warming occurs when winds and turbulent fluxes are weak, thus it reduces intraseasonal variability of surface fluxes (de Szoeke and Edson 2014). The diurnal warm layer makes the maximum SST occur a few days earlier than the mixed layer temperature, which could contribute to the MJO by enhancing heat fluxes and frictional convergence ahead of the convective phase.

The moisture recharge conceptual model depends on moisture building up in the atmosphere in advance of the convective phase of the MJO. In an analysis of tropical soundings and reanalysis, Kemball-Cook and Weare (2001) found a moisture increase and convergence ($-\nabla \cdot \mathbf{u}$) ahead of convection for equatorial locations. Their analysis and the DYNAMO–*Revelle* equatorial time series support the frictional wave-CISK theory in which frictional boundary layer convergence destabilizes convective waves within a narrow band near the equator. Off the equator, they found convergence was synchronous with convection rather than with increasing moisture. Though horizontal convergence is not equivalent to moisture advection, the lack of convergence off the equator led Kemball-Cook and Weare (2001) to propose that moisture recharge by local evaporation there preconditioned the atmosphere for deep convection.

While there is local evaporation, the processes responsible for moistening are very unlikely to be purely local, on or off the equator. Observations show evaporation is relatively constant at about half the mean precipitation over the warm equatorial regions of the Indian and Pacific Oceans. Thus, on the whole, moisture must converge horizontally into the region. Synoptic convectively coupled Kelvin–Rossby waves comprise intense convective rain events within the MJO in DYNAMO and TOGA COARE. The days of strongest rain exceed evaporation by an order of magnitude and yield an increase in column-integrated moisture (Fig. 9). This implies that anomalous column moisture flux convergence is important for the MJO and its embedded convective storms. The moisture budget does not distinguish whether the moisture convergence is the cause or the consequence of precipitating synoptic storms. Even if the moisture convergence is not the cause of precipitation, the similar magnitude of synoptic convergence and precipitation still suggests that the aggregate of precipitation from storms is related to convergence in the MJO. The requirement for moisture convergence to balance the local moisture budget on daily and long-term mean time scales leads us to expect that moisture convergence is important to supply moisture to precipitation in the MJO convective phase. The moisture contributed steadily by evaporation is absolutely critical to the tropical circulation, the MJO, and the convective storms. The accumulation of moisture over time and the convergence of moisture over space determine exactly when, where, and how much it rains.

With only three intraseasonal realizations from the ship in DYNAMO, we cannot clearly distinguish intraseasonal recharge from synoptic discharge of moisture anomalies. The increase of column moisture during the inactive phase supports the recharge mechanism for MJO convection, but the same magnitude increase of moisture during the strongest precipitation suggests that the interaction of convection with the column moisture is more complicated than the simple moisture recharge paradigm.

DYNAMO sampled the MJO in the central Indian Ocean at the completion of its early genesis phase and the beginning of its mature phase where intraseasonal OLR and surface flux variables reach their maximum amplitude. Air–sea interaction may be different in the earlier genesis of the MJO in the western Indian Ocean, where intraseasonal SST responds more sensitively to the net surface flux. The large region of enhanced westerly wind and evaporation anomalies in the western Indian Ocean may contribute to the MJO when it is growing in the central Indian Ocean.

Acknowledgments. We thank the three anonymous reviewers. Their helpful and timely reviews significantly improved this work. We thank Sergio Pezoa, Kenneth Moran, Daniel Wolfe, Raymond Kreth, Sasha Perlin, and the crew of the R/V *Roger Revelle*, without whom collecting these observations would not have been possible. TOGA COARE air–sea fluxes and sea surface data are provided by the Research Data Archive at the National Center for Atmospheric Research, Computational and Information Systems Laboratory (http://rda.ucar.edu/datasets/ds606.1/). Interpolated OLR data are provided by the NOAA/OAR/ESRL/PSD, Boulder, Colorado (http://www.esrl.noaa.gov/psd/). OAFlux data are graciously provided by Woods Hole Oceanographic Institution (http://oaflux.whoi.edu/). The TropFlux data are produced under a collaboration between Laboratoire d'Océanographie: Expérimentation et Approches Numériques (LOCEAN) from Institute Pierre-Simon Laplace (IPSL, Paris, France) and National Institute of Oceanography/CSIR (NIO, Goa, India), and supported by Institut de Recherche pour le Développement (IRD, France). ISCCP FD data are available at http://isccp.giss.nasa.gov/projects/flux.html. We gratefully acknowledge support from NOAA OAR Grants NA11OAR4310076 and NA13OAR4310160, and ONR Grants N00014-10-1-0299, N00014-10-1-0546, and N00014-14-1-0140.

APPENDIX A

Description of the DYNAMO Data

In situ meteorology and high-rate flux sensors operated continuously during the four legs of the DYNAMO experiment. Continuous 1- and 10-min resolution time series of meteorological means, fluxes, related measurements, and derived data, from the R/V *Roger Revelle* DYNAMO research cruises are available at ftp://dynamo.dms.uconn.edu/, and linked from the DYNAMO field catalog http://catalog.eol.ucar.edu/dynamo/. Data were sampled at the frequencies and heights specified in Table A1 and variables are adjusted to standard heights of 2 or 10 m using Monin–Obukhov similarity accounting for hydrostatic pressure and adiabatic temperature changes.

a. Wind speed

Velocity is measured by three sonic anemometers deployed on the forward mast by NOAA/ESRL/PSD, UConn, and OSU. The wind speeds are averaged from the sensor(s) best exposed to the wind, depending on the relative wind direction. Aside from buoy deployment activities during leg 1, the *Revelle* was usually positioned with the bow pointing into the mean current to allow oceanic microstructure profiling from the fantail, providing relative wind directions within ±90° of the bow

TABLE A1. Summary of primary instrumentation on the *Revelle* in DYNAMO.

Sensor	Variable(s) measured	Manufacturer and model	Sampling frequency (Hz)	Height (m)
Sonic anemometer	Three-axis wind components and sonic temperature	Gill R3–100	10	17.8
		Gill R3–50	10	17.5
		Campbell CSAT3	20	16.9
Infrared gas analyzer	Water vapor	Licor LI-7500	10	17.2
Inertial motion unit	Linear accelerations and angular rates	Systron Donner MotionPak	10 and 20	17.0
		Systron Donner MotionPakII	10	16.6
GPS compass	Heading	Hemisphere Crescent VS100	10	12.2
				16.9
Aspirated *T*/RH	Air temperature and relative humidity	Vaisala HMT 335	0.1	15.6
		Vaisala PTU 200	1	16.2
Barometer	Air pressure	Vaisala PTU 200	1	8.6
Pyranometer	Solar (shortwave) radiative flux	Eppley PSP	Unknown	20.4
		Kipp & Zonen CM21	1	13
Pyrgeometer	IR (longwave) radiative flux	Eppley PIR	Unknown	20.4
		Eppley PIR	0.1	12.6
		Kipp & Zonen CG4	1	13
Optical rain gauge	Rainfall rate	STI ORG	0.1	16.5
Self-siphoning rain gauge	Rainfall	RM Young 50202	1	16.5
Laser altimeter	Wave height	Riegl LD90–3100VHS-FLP	10 Hz	18.5
Sea-snake thermistor	Sea temperature	YSI – 44030	0.1 Hz	−0.1
Thermosalino-graph	Sea temperature and salinity	SeaBird SBE 45 MicroTSG	Unknown	−4.9
ADCP	Ocean currents	RDI Narrowband 150 kHz	Unknown	−25

for 81% of the time and ±135° of the bow for 93% of the time. Winds were excluded from relative wind directions outside ±135°. The winds are corrected for flow distortion using an empirical correction based on comparisons with nearby buoys and lidar-derived winds.

b. Temperature, pressure, and humidity

Two aspirated temperature/relative humidity sensors on the bow mast measured air temperature (T) and relative humidity (RH). measurements of T and RH are processed to remove heat contamination of the ship during daylight. We postcalibrated the T/RH sensors in either a calibration chamber at UConn, or at the manufacturer (Vaisala); both calibrations agree. The ESRL/PSD temperature sensor had the most effective aspirator and the least contamination by solar heating. In one period its fan failed and the aspirated UConn temperature sensor was used. Specific humidity and air pressure are computed from the aspirated UConn T/RH and pressure sensors. Specific humidity is less sensitive to solar heating as long as the temperature and RH are measured simultaneously. RH is then reconstructed from the specific humidity, pressure and the best estimate of the air temperature.

c. Sea temperature, salinity, and currents

Near-surface sea temperature was measured by the "sea snake" comprising a towed thermistor floating approximately 5 cm beneath the surface. The sea-snake measurements are reduced by 0.058°C based on a comparison with a subsurface temperature chain deployed by OSU ocean mixing group as described in Moum et al. (2014). The water interface temperature is computed from the sea-snake adjusted for the effects of the viscous cool skin (Saunders 1967; Fairall et al. 1996a). Sea surface temperatures were additionally estimated by radiometric measurements of skin temperature (C. Zappa 2014, Lamont-Doherty Earth Observatory, personal communication). These SST estimates filled gaps during the first 11 days of leg 2 when problems were encountered with the sea-snake measurements. Values of the temperature and salinity are also measured at approximately 4.9-m depth by the ship's intake thermosalinograph. Surface currents were collected from the ship's Acoustic Doppler Current Profiler (ADCP) and quality control by the OSU ocean mixing group (Moum et al. 2014).

d. Precipitation

Precipitation was provided by the ERSL/PSD optical rain gauge located on the forward mast after calibration with five catchment rain gauges deployed by OSU, UConn, and the meteorological sensors of the *Revelle*. All catchment rain gauges were in good agreement during periods of low winds. The optical rain gauge was correlated well, but was adjusted by a factor of 1.4 to agree with the mean rain rate of the other gauges. During periods of high winds, the manual and self-siphoning rain gauges appeared to underestimate the

daily precipitation compared to the adjusted optical rain gauge. Presumably, this is due to the effect of flow distortion on the rain gauges. The optical rain had good exposure on the forward mast and lower sensitivity to wind. Therefore, the adjusted rain rate from the optical rain gauge is used as the in situ time series of precipitation from the *Revelle*. The adjusted rain rate from the optical rain gauge agrees well with nearby buoy measurements.

e. Radiative fluxes

The downwelling thermal infrared (IR) radiation is computed using an average of the motion-stabilized ESRL/PSD pyrgeometers mounted above the O2 deck and the ship's pyrgeometer on the top of the forward mast. The pyrgeometers are corrected for the effects of solar heating. The upwelling IR radiation is modeled from the SST computed from the sea-snake, accounting for emission and reflection using an emissivity, $\varepsilon = 0.97$. Downwelling solar radiation is measured by the ship's pyranometer on the top of the forward mast. The upwelling solar radiation is computed from a commonly used parameterization for surface albedo of the ocean as a function of solar altitude (Payne 1972).

Measurements of the diffuse solar radiation are made by a National Center for Atmospheric Research (NCAR) sunshine pyranometer (SPN1; Delta-T Devices Ltd) deployed on the top of the forward mast. Clear-sky solar radiation (i.e., and atmosphere with no clouds) is estimated by a model adapted from Iqbal (1988) for total solar irradiance ($1367\,\mathrm{W\,m^{-2}}$), solar zenith angle, and absorption and scattering by gases, aerosols, ozone, and water vapor; and tuned to match observations on clear days.

f. Surface fluxes of heat, mass, and momentum

The optimized set of mean meteorological and surface ocean measurements (wind, temperature, and currents) are used to compute the latent, sensible, and rain fluxes with the COARE 3.5 algorithm (Fairall et al. 1996b; Fairall et al. 2003; Edson et al. 2013), using the wind speed relative to the ocean surface. The transfer coefficients in COARE 3.5 have been adjusted to match the heat fluxes given by COARE 3.0. Continued improvement and validation of the COARE algorithm is a goal of the experiment, and ESRL/PSD, UConn, and OSU deployed turbulence flux instrumentation (sonic anemometers and infrared gas analyzers) to compute fluxes with the eddy correlation method.

g. Atmospheric remote sensing

In addition to the flux system there were three upward-looking remote systems operated by ESRL/PSD: a mechanically stabilized W-Band Doppler cloud radar (Moran et al. 2012), a two-channel (23 and 31 GHz) microwave radiometer, and a lidar ceilometer. The W-band cloud radar sampled clouds and precipitation in low-altitude mode (0–7 km) when on station at the equator, and in high-altitude mode (0–14 km) when the *Revelle* was in transit. The microwave radiometer sampled column liquid water and water vapor path, and the ceilometers sampled cloud-base heights and uncalibrated optical backscatter. These remote sensing measurements have been analyzed to retrieve hourly cloud properties such as cloud liquid water concentration, cloud-top height, and cloud-base height. These values are available at ftp://ftp1.esrl.noaa.gov/psd3/cruises/DYNAMO_2011/Revelle/radar/wband/processed/.

h. Surface wave measurements

A laser altimeter was pointed forward of the forward mast to provide measurements of the surface wave field during DYNAMO legs 2–4. It provides hourly estimates of the significant wave height and phase speed of the dominant waves from the frequency at the spectral peak between 0.01 and 0.5 Hz.

APPENDIX B

Principal Component Analysis Procedure

We use a PCA method to decompose the intraseasonally filtered time–longitude structure of OLR into an efficient representation of the MJO, and to find the surface flux expression of the MJO. The PCA is quite standard and similar to that used by others to describe the MJO (e.g., Shinoda et al. 1998). Our unique event identification and compositing method relies on the PCA, so we briefly introduce the PCA here. The intraseasonally filtered time series–longitude matrix (e.g., of OLR) $\mathbf{X}_*$ can be written as a product using singular value decomposition:

$$\mathbf{X}_* = \mathbf{U}\mathbf{\Sigma}\mathbf{V}^{\mathrm{T}} = \mathbf{P}_*\mathbf{F}_*, \tag{B1}$$

where the superscript T stands for the matrix transpose. Other numerical methods for the PCA (e.g., eigenvector decomposition of the covariance matrix) are equivalent. The columns of $\mathbf{P}_* = N^{1/2}\mathbf{U}$ are the unity-variance normalized principal component time series. The variable N is the number of samples (days). The rows of $\mathbf{F}_* = N^{-1/2}\mathbf{\Sigma}\mathbf{V}^{\mathrm{T}}$ are the empirical orthogonal functions of longitude. A row of $\mathbf{F}_*$ has the same units as $\mathbf{X}_*$ (e.g., $\mathrm{W\,m^{-2}}$ for OLR) and represents the spatial pattern realized by a standard deviation of 1 in the corresponding PC time series.

We truncate the expansion $\mathbf{P}_*$ and $\mathbf{F}_*$ to the first two principal component time series $\mathbf{P} = [\mathbf{P}_1\ \mathbf{P}_2]$ and the first two empirical orthogonal functions $\mathbf{F}$. The truncated time-longitude series explained by the first two PCs is

$$\mathbf{X} = \mathbf{PF}. \tag{B2}$$

In analogy to $\mathbf{F}$, the spatial pattern $\mathbf{G}$ of another variable (e.g., surface flux) $\mathbf{Y}_*$ explained by the principal component can be generated by projection (regression) onto the truncated principal component $\mathbf{P}$:

$$\mathbf{G} = \mathbf{P}^{\mathrm{T}}\mathbf{Y}_*. \tag{B3}$$

Analogous to $\mathbf{X}$, the truncated time–space variability of $\mathbf{Y}_*$ associated with the first two PCs and, hence, the MJO is

$$\mathbf{Y} = \mathbf{PG} = \mathbf{P}(\mathbf{P}^{\mathrm{T}}\mathbf{Y}). \tag{B4}$$

a. *Event identification*

Surface sea–air fluxes were composited in MJO events. MJO events were defined by the two-dimensional state space of the first two normalized PC time series. The phase ϕ of the MJO at time t is

$$\phi = \tan^{-1}[P_2(t)/P_1(t)]. \tag{B5}$$

MJO events are defined by the vector (P_1, P_2), according to PC amplitudes meeting thresholds and progressing eastward (e.g., $P_1 < -1.5$ followed by $P_1 > 0$ and $P_2 < -1.5$ within 25 days; Shinoda et al. 1998). Some strong OLR anomalies, including the DYNAMO convective events, did not meet these thresholds. We used another criterion based on the integrated area swept out by the eastward-phase progression of PC1 and PC2 to identify MJO events. The area of a sector of (P_1, P_2) space swept out between successive days is

$$\frac{|\mathbf{P}^2|}{2}d\phi, \tag{B6}$$

where $|\mathbf{P}^2| = P_1^2 + P_2^2$ is the square of the magnitude of the vector (P_1, P_2), and the phase angle between successive days $\mathbf{P}^-$ and $\mathbf{P}^+$ is

$$d\phi = \tan^{-1}\left(\frac{P_1^- P_2^+ - P_2^- P_1^+}{P_1^- P_1^+ - P_2^- P_2^+}\right). \tag{B7}$$

Positive $d\phi$ corresponds to eastward propagation of OLR anomalies.

MJO events are identified when the area of the sector swept out by the normalized vector in (P_1, P_2) space over 25 days is greater than $\pi/2$. This area is equivalent to that of a semicircle with a radius of one standard deviation. This condition identifies events that propagate eastward with significant amplitude. The condition identifies 103 events in the 27.5 yr of OLR data analyzed.

b. *Compositing by intraseasonal phase*

The phase depends on the arbitrary signs of P_1 and P_2. For our P_1 and P_2 there are negative intraseasonal OLR anomalies over the central Indian Ocean when $P_1 < 0$ and $P_2 = 0$. If the centered 25-day integral satisfies the above criterion, the day that $P_1 < 0$ and $P_2 = 0$ is identified as day 0 ($\phi = 0$) of the event. The daily unfiltered 15°S–15°N average OLR and surface variables within ±60 days of day 0 are then composited on the phase of the OLR PC index. Daily data in the 60 days prior to day 0 are assigned to one of 24 phase bins corresponding to the cycle preceding day zero. Data in the 60 days following day zero are assigned to one of 24 phase bins after event day zero. Days are not composited for a time difference of more than 60 days or for a phase difference more than 2π. In this way we composite two intraseasonal cycles for each event, one before and one after $\phi = 0$ when the maximum amplitude is obtained in the central Indian Ocean.

REFERENCES

Anderson, S. P., R. A. Weller, and R. B. Lukas, 1996: Surface buoyancy forcing and the mixed layer of the western Pacific warm pool: Observations and 1D model results. *J. Climate,* **9,** 3056–3085, doi:10.1175/1520-0442(1996)009<3056:SBFATM>2.0.CO;2.

Back, L. E., and C. S. Bretherton, 2009: On the relationship between SST gradients, boundary layer winds, and convergence over the tropical oceans. *J. Climate,* **22,** 4182–4196, doi:10.1175/2009JCLI2392.1.

Benedict, J. J., and D. A. Randall, 2007: Observed characteristics of the MJO relative to maximum rainfall. *J. Atmos. Sci.,* **64,** 2332–2354, doi:10.1175/JAS3968.1.

——, and ——, 2009: Structure of the Madden–Julian oscillation in the superparameterized CAM. *J. Atmos. Sci.,* **66,** 3277–3296, doi:10.1175/2009JAS3030.1.

——, and ——, 2011: Impacts of idealized air–sea coupling on Madden–Julian oscillation structure in the superparameterized CAM. *J. Atmos. Sci.,* **68,** 1990–2008, doi:10.1175/JAS-D-11-04.1.

——, E. D. Maloney, A. H. Sobel, and D. M. W. Frierson, 2014: Gross moist stability and MJO simulation skill in three full-physics GCMs. *J. Atmos. Sci.,* **71,** 3327–3349, doi:10.1175/JAS-D-13-0240.1.

Bladé, I., and D. L. Hartmann, 1993: Tropical intraseasonal oscillations in a simple nonlinear model. *J. Atmos. Sci.,* **50,** 2922–2939, doi:10.1175/1520-0469(1993)050<2922:TIOIAS>2.0.CO;2.

Dee, D. P., and Coauthors, 2011: The ERA-Interim reanalysis: Configuration and performance of the data assimilation system. *Quart. J. Roy. Meteor. Soc.,* **137,** 553–597, doi:10.1002/qj.828.

DeMott, C. A., C. Stan, D. A. Randall, and M. D. Branson, 2014: Intraseasonal variability in coupled GCMs: The roles of ocean

feedbacks and model physics. *J. Climate,* **27,** 4970–4995, doi:10.1175/JCLI-D-13-00760.1.

de Szoeke, S. P., and J. B. Edson, 2014: Intraseasonal air–sea interaction and convection observed in DYNAMO/CINDY/AMIE. *The Global Monsoon System: Research and Forecast,* C. P. Chang, Ed., World Scientific, in press.

Donlon, C. J., M. Martin, J. Stark, J. Roberts-Jones, E. Fiedler, and W. Wimmer, 2012: The Operational Sea Surface Temperature and Sea Ice Analysis (OSTIA) system. *Remote Sens. Environ.,* **116,** 140–158, doi:10.1016/j.rse.2010.10.017.

Edson, J. B., and Coauthors, 2013: On the exchange of momentum over the open ocean. *J. Phys. Oceanogr.,* **43,** 1589–1610, doi:10.1175/JPO-D-12-0173.1.

Emanuel, K. A., 1987: An air–sea interaction model of intraseasonal oscillations in the tropics. *J. Atmos. Sci.,* **44,** 2324–2340, doi:10.1175/1520-0469(1987)044<2324:AASIMO>2.0.CO;2.

Fairall, C. W., E. F. Bradley, J. S. Godfrey, G. A. Wick, J. B. Edson, and G. S. Young, 1996a: Cool-skin and warm-layer effects on sea surface temperature. *J. Geophys. Res.,* **101,** 1295–1308, doi:10.1029/95JC03190.

——, ——, D. P. Rogers, J. B. Edson, and G. S. Young, 1996b: Bulk parameterization of air-sea fluxes for Tropical Ocean-Global Atmosphere Coupled-Ocean Atmosphere Response Experiment. *J. Geophys. Res.,* **101,** 3747–3764, doi:10.1029/95JC03205.

——, A. B. White, J. B. Edson, and J. E. Hare, 1997: Integrated shipboard measurements of the marine boundary layer. *J. Atmos. Oceanic Technol.,* **14,** 338–359, doi:10.1175/1520-0426(1997)014<0338:ISMOTM>2.0.CO;2.

——, E. F. Bradley, J. E. Hare, A. A. Grachev, and J. B. Edson, 2003: Bulk parameterization of air–sea fluxes: Updates and verification for the COARE algorithm. *J. Climate,* **16,** 571–591, doi:10.1175/1520-0442(2003)016<0571:BPOASF>2.0.CO;2.

Flatau, M., P. J. Flatau, P. Phoebus, and P. P. Niiler, 1997: The feedback between equatorial convection and local radiative and evaporative processes: The implications for intraseasonal oscillations. *J. Atmos. Sci.,* **54,** 2373–2386, doi:10.1175/1520-0469(1997)054<2373:TFBECA>2.0.CO;2.

Gill, A. E., 1980: Some simple solutions for heat-induced tropical circulation. *Quart. J. Roy. Meteor. Soc.,* **106,** 447–462, doi:10.1002/qj.49710644905.

Hannah, W. M., and E. D. Maloney, 2014: The moist static energy budget in NCAR CAM5 hindcasts during DYNAMO. *J. Adv. Model. Earth Syst.,* **6,** 420–440, doi:10.1002/2013MS000272.

Hendon, H. H., 2005: Air-sea interaction. *Intraseasonal Variability in the Atmosphere-Ocean Climate System,* W. K. M. Lau and D. E. Waliser, Eds., Springer, 223–246.

——, and M. L. Salby, 1994: The life cycle of the Madden–Julian oscillation. *J. Atmos. Sci.,* **51,** 2225–2237, doi:10.1175/1520-0469(1994)051<2225:TLCOTM>2.0.CO;2.

——, and J. Glick, 1997: Intraseasonal air–sea interaction in the tropical Indian and Pacific Oceans. *J. Climate,* **10,** 647–661, doi:10.1175/1520-0442(1997)010<0647:IASIIT>2.0.CO;2.

Inness, P. M., and J. M. Slingo, 2003: Simulation of the Madden–Julian oscillation in a coupled general circulation model. Part I: Comparison with observations and an atmosphere-only GCM. *J. Climate,* **16,** 345–364, doi:10.1175/1520-0442(2003)016<0345:SOTMJO>2.0.CO;2.

Iqbal, M., 1988: Spectral and total sun radiance under cloudless skies. *Physical Climatology for Solar and Wind Energy,* R. Guzzi and C. G. Justus, Eds., World Scientific, 196–242.

Johnson, R. H., and P. E. Ciesielski, 2013: Structure and properties of Madden–Julian oscillations deduced from DYNAMO sounding arrays. *J. Atmos. Sci.,* **70,** 3157–3179, doi:10.1175/JAS-D-13-065.1.

——, T. M. Rickenbach, S. A. Rutledge, P. E. Ciesielski, and W. H. Schubert, 1999: Trimodal characteristics of tropical convection. *J. Climate,* **12,** 2397–2418, doi:10.1175/1520-0442(1999)012<2397:TCOTC>2.0.CO;2.

——, P. E. Ciesielski, J. H. Ruppert, and M. Katsumata, 2014: Sounding-based thermodynamic budgets for DYNAMO. *J. Atmos. Sci.,* doi:10.1175/JAS-D-14-0202.1, in press.

Kalnay, E., and Coauthors, 1996: The NCEP/NCAR 40-Year Reanalysis Project. *Bull. Amer. Meteor. Soc.,* **77,** 437–471, doi:10.1175/1520-0477(1996)077<0437:TNYRP>2.0.CO;2.

Kanamitsu, M., W. Ebisuzaki, J. Woollen, S.-K. Yang, J. J. Hnilo, M. Fiorino, and G. L. Potter, 2002: NCEP–DOE AMIP-II reanalysis (R-2). *Bull. Amer. Meteor. Soc.,* **83,** 1631–1643, doi:10.1175/BAMS-83-11-1631.

Kemball-Cook, S. R., and B. C. Weare, 2001: The onset of convection in the Madden–Julian oscillation. *J. Climate,* **14,** 780–793, doi:10.1175/1520-0442(2001)014<0780:TOOCIT>2.0.CO;2.

Kiladis, G. N., M. C. Wheeler, P. T. Haertel, K. H. Straub, and P. E. Roundy, 2009: Convectively coupled equatorial waves. *Rev. Geophys.,* **47,** RG2003, doi:10.1029/2008RG000266.

——, and Coauthors, 2014: A comparison of OLR and circulation-based indices for tracking the MJO. *Mon. Wea. Rev.,* **142,** 1697–1715, doi:10.1175/MWR-D-13-00301.1.

Krishnamurti, T. N., D. K. Oosterhof, and A. V. Mehta, 1988: Air-sea interaction on the time scale of 30 to 50 days. *J. Atmos. Sci.,* **45,** 1304–1322, doi:10.1175/1520-0469(1988)045<1304:AIOTTS>2.0.CO;2.

Lau, K.-M., and L. Peng, 1987: Origin of low-frequency (intraseasonal) oscillations in the tropical atmosphere. Part I: Basic theory. *J. Atmos. Sci.,* **44,** 950–972, doi:10.1175/1520-0469(1987)044<0950:OOLFOI>2.0.CO;2.

Liebmann, B., and C. A. Smith, 1996: Description of a complete (interpolated) outgoing longwave radiation dataset. *Bull. Amer. Meteor. Soc.,* **77,** 1275–1277.

Lin, X., and R. H. Johnson, 1996: Heating, moistening, and rainfall over the western Pacific warm pool during TOGA COARE. *J. Atmos. Sci.,* **53,** 3367–3383, doi:10.1175/1520-0469(1996)053<3367:HMAROT>2.0.CO;2.

Lindzen, R. S., and S. Nigam, 1987: On the role of sea surface temperature gradients in forcing low-level winds and convergence in the tropics. *J. Atmos. Sci.,* **44,** 2418–2436, doi:10.1175/1520-0469(1987)044<2418:OTROSS>2.0.CO;2.

Madden, R. A., and P. R. Julian, 1971: Detection of a 40–50 day oscillation in the zonal wind in the tropical Pacific. *J. Atmos. Sci.,* **28,** 702–708, doi:10.1175/1520-0469(1971)028<0702:DOADOI>2.0.CO;2.

Majda, A. J., and S. N. Stechmann, 2009: The skeleton of tropical intraseasonal oscillations. *Proc. Natl. Acad. Sci. USA,* **106,** 8417–8422, doi:10.1073/pnas.0903367106.

Maloney, E. D., 2009: The moist static energy budget of a composite tropical intraseasonal oscillation in a climate model. *J. Climate,* **22,** 711–729, doi:10.1175/2008JCLI2542.1.

——, and D. L. Hartmann, 1998: Frictional moisture convergence in a composite life cycle of the Madden–Julian oscillation. *J. Climate,* **11,** 2387–2403, doi:10.1175/1520-0442(1998)011<2387:FMCIAC>2.0.CO;2.

——, and J. T. Kiehl, 2002: MJO-related SST variations over the tropical eastern Pacific during Northern Hemisphere summer. *J. Climate,* **15,** 675–689, doi:10.1175/1520-0442(2002)015<0675:MRSVOT>2.0.CO;2.

——, and A. H. Sobel, 2004: Surface fluxes and ocean coupling in the tropical intraseasonal oscillation. *J. Climate,* **17,** 4368–4386, doi:10.1175/JCLI-3212.1.

Marion, J. R., 2014: Providing the best turbulent heat flux estimates from eddy correlation and bulk methods using DYNAMO data. M.S. thesis, College of Earth, Ocean, and Atmospheric Sciences, Oregon State University, 167 pp.

Marshall, A. G., O. Alves, and H. H. Hendon, 2008: An enhanced moisture convergence–evaporation feedback mechanism for MJO air–sea interaction. *J. Atmos. Sci.,* **65,** 970–986, doi:10.1175/2007JAS2313.1.

McPhaden, M. J., F. Bahr, Y. Du Penhoat, E. Firing, S. P. Hayes, P. P. Niiler, P. L. Richardson, and J. M. Toole, 1992: The response of the western equatorial Pacific Ocean to westerly wind bursts during November 1989 to January 1990. *J. Geophys. Res.,* **97,** 14 289–14 303, doi:10.1029/92JC01197.

Moran, K. P., S. Pezoa, C. Fairall, C. Williams, T. Ayers, A. Brewer, S. P. de szoeke, and V. Ghate, 2012: A motion-stabilized W-band radar for shipboard observations of marine boundary layer clouds. *Bound.-Layer Meteor.,* **143,** 3–24, doi:10.1007/s10546-011-9674-5.

Moum, J. N., and Coauthors, 2014: Air–sea interactions from westerly wind bursts during the November 2011 MJO in the Indian Ocean. *Bull. Amer. Meteor. Soc.,* **95,** 1185–1199, doi:10.1175/BAMS-D-12-00225.1

Neelin, J. D., and N. Zeng, 2000: A quasi-equilibrium tropical circulation model—Formulation. *J. Atmos. Sci.,* **57,** 1741–1766, doi:10.1175/1520-0469(2000)057<1741:AQETCM>2.0.CO;2.

——, I. M. Held, and K. H. Cook, 1987: Evaporation–wind feedback and low-frequency variability in the tropical atmosphere. *J. Atmos. Sci.,* **44,** 2341–2348, doi:10.1175/1520-0469(1987)044<2341:EWFALF>2.0.CO;2.

North, G. R., T. L. Bell, R. F. Cahalan, and F. J. Moeng, 1982: Sampling errors in the estimation of empirical orthogonal functions. *Mon. Wea. Rev.,* **110,** 699–706, doi:10.1175/1520-0493(1982)110<0699:SEITEO>2.0.CO;2.

Payne, R. E., 1972: Albedo of the sea surface. *J. Atmos. Sci.,* **29,** 959–970, doi:10.1175/1520-0469(1972)029<0959:AOTSS>2.0.CO;2.

Praveen Kumar, B., J. Vialard, M. Lengaigne, V. S. N. Murty, and M. J. McPhaden, 2012: TropFlux: Air-sea fluxes for the global tropical oceans—Description and evaluation. *Climate Dyn.,* **38,** 1521–1543, doi:10.1007/s00382-011-1115-0.

Price, J. F., R. A. Weller, and R. Pinkel, 1986: Diurnal cycling: Observations and models of the upper ocean response to diurnal heating, cooling, and wind mixing. *J. Geophys. Res.,* **91,** 8411–8427, doi:10.1029/JC091iC07p08411.

Reynolds, R. W., N. A. Rayner, T. M. Smith, D. C. Stokes, and W. Wang, 2002: An improved in situ and satellite SST analysis for climate. *J. Climate,* **15,** 1609–1625, doi:10.1175/1520-0442(2002)015<1609:AIISAS>2.0.CO;2.

——, T. M. Smith, C. Liu, D. B. Chelton, K. S. Casey, and M. G. Schlax, 2007: Daily high-resolution-blended analyses for sea surface temperature. *J. Climate,* **20,** 5473–5496, doi:10.1175/2007JCLI1824.1.

Riehl, H., and J. S. Malkus, 1958: On the heat balance in the equatorial trough zone. *Geophysica,* **6,** 503–538.

Risien, C. M., and D. B. Chelton, 2008: A global climatology of surface wind and wind stress fields from eight years of QuikSCAT scatterometer data. *J. Phys. Oceanogr.,* **38,** 2379–2413, doi:10.1175/2008JPO3881.1.

Rui, H., and B. Wang, 1990: Development characteristics and dynamic structure of tropical intraseasonal convection anomalies. *J. Atmos. Sci.,* **47,** 357–379, doi:10.1175/1520-0469(1990)047<0357:DCADSO>2.0.CO;2.

Salby, M. L., R. R. Garcia, and H. H. Hendon, 1994: Planetary-scale circulations in the presence of climatological and wave-induced heating. *J. Atmos. Sci.,* **51,** 2344–2367, doi:10.1175/1520-0469(1994)051<2344:PSCITP>2.0.CO;2.

Saunders, P. M., 1967: The temperature at the ocean-air interface. *J. Atmos. Sci.,* **24,** 269–273, doi:10.1175/1520-0469(1967)024<0269:TTATOA>2.0.CO;2.

Shinoda, T., H. H. Hendon, and J. Glick, 1998: Intraseasonal variability of surface fluxes and sea surface temperature in the tropical western Pacific and Indian Oceans. *J. Climate,* **11,** 1685–1702, doi:10.1175/1520-0442(1998)011<1685:IVOSFA>2.0.CO;2.

Smyth, W. D., D. Hebert, and J. N. Moum, 1996: Local ocean response to a multiphase westerly wind burst: 2. Thermal and freshwater responses. *J. Geophys. Res.,* **101,** 22 513–22 533, doi:10.1029/96JC02006.

Sobel, A. H., and C. S. Bretherton, 2000: Modeling tropical precipitation in a single column. *J. Climate,* **13,** 4378–4392, doi:10.1175/1520-0442(2000)013<4378:MTPIAS>2.0.CO;2.

——, and E. Maloney, 2012: An idealized semi-empirical framework for modeling the Madden–Julian oscillation. *J. Atmos. Sci.,* **69,** 1691–1705, doi:10.1175/JAS-D-11-0118.1.

——, J. Nilsson, and L. M. Polvani, 2001: The weak temperature gradient approximation and balanced tropical moisture waves. *J. Atmos. Sci.,* **58,** 3650–3665, doi:10.1175/1520-0469(2001)058<3650:TWTGAA>2.0.CO;2.

——, E. D. Maloney, G. Bellon, and D. M. Frierson, 2010: Surface fluxes and tropical intraseasonal variability: A reassessment. *J. Adv. Model. Earth Syst.,* **2** (27), doi:10.3894/JAMES.2010.2.2.

Straub, K. H., and G. N. Kiladis, 2003: The observed structure of convectively coupled Kelvin waves: Comparison with simple models of coupled wave instability. *J. Atmos. Sci.,* **60,** 1655–1668, doi:10.1175/1520-0469(2003)060<1655:TOSOCC>2.0.CO;2.

Sugiyama, M., 2009: The moisture mode in the quasi-equilibrium tropical circulation model. Part I: Analysis based on the weak temperature gradient approximation. *J. Atmos. Sci.,* **66,** 1507–1523, doi:10.1175/2008JAS2690.1.

Uppala, S. M., and Coauthors, 2005: The ERA-40 Re-Analysis. *Quart. J. Roy. Meteor. Soc.,* **131,** 2961–3012, doi:10.1256/qj.04.176.

Waliser, D. E., 2006: Intraseasonal variability. *The Asian Monsoon,* B. Wang, Ed., Springer, 203–257.

——, K. M. Lau, and J.-H. Kim, 1999: The influence of coupled sea surface temperatures on the Madden–Julian oscillation: A model perturbation experiment. *J. Atmos. Sci.,* **56,** 333–358, doi:10.1175/1520-0469(1999)056<0333:TIOCSS>2.0.CO;2.

Wang, B., and H. Rui, 1990: Dynamics of the coupled moist Kelvin–Rossby wave on an equatorial β-plane. *J. Atmos. Sci.,* **47,** 397–413, doi:10.1175/1520-0469(1990)047<0397:DOTCMK>2.0.CO;2.

——, and X. Xie, 1998: Coupled modes of the warm pool climate system. Part I: The role of air–sea interaction in maintaining Madden–Julian oscillation. *J. Climate,* **11,** 2116–2135, doi:10.1175/1520-0442-11.8.2116.

Webster, P. J., and R. Lukas, 1992: TOGA COARE: The Coupled Ocean–Atmosphere Response Experiment. *Bull. Amer. Meteor. Soc.,* **73,** 1377–1416, doi:10.1175/1520-0477(1992)073<1377:TCTCOR>2.0.CO;2.

Weller, R. A., and S. P. Anderson, 1996: Surface meteorology and air-sea fluxes in the western equatorial Pacific warm pool during the TOGA Coupled Ocean-Atmosphere Response

Experiment. *J. Climate,* **9,** 1959–1990, doi:10.1175/1520-0442(1996)009<1959:SMAASF>2.0.CO;2.

Wheeler, M. C., and G. N. Kiladis, 1999: Convectively coupled equatorial waves: Analysis of clouds and temperature in the wavenumber-frequency domain. *J. Atmos. Sci.,* **56,** 374–399, doi:10.1175/1520-0469(1999)056<0374:CCEWAO>2.0.CO;2.

——, and H. H. Hendon, 2004: An all-season Real-Time Multivariate MJO index: Development of an index for monitoring and prediction. *Mon. Wea. Rev.,* **132,** 1917–1932, doi:10.1175/1520-0493(2004)132<1917:AARMMI>2.0.CO;2.

Woodruff, S., H. Diaz, J. Elms, and S. Worley, 1998: COADS release 2 data and metadata enhancements for improvements of marine surface flux fields. *Phys. Chem. Earth,* **23,** 517–526, doi:10.1016/S0079-1946(98)00064-0.

Woolnough, S. J., J. M. Slingo, and B. J. Hoskins, 2000: The relationship between convection and sea surface temperature on intraseasonal timescales. *J. Climate,* **13,** 2086–2104, doi:10.1175/1520-0442(2000)013<2086:TRBCAS>2.0.CO;2.

——, F. Vitart, and M. A. Balmaseda, 2007: The role of the ocean in the Madden–Julian Oscillation: Implications for MJO prediction. *Quart. J. Roy. Meteor. Soc.,* **133,** 117–128, doi:10.1002/qj.4.

Yang, D., and A. P. Ingersoll, 2013: Triggered convection, gravity waves, and the MJO: A shallow-water model. *J. Atmos. Sci.,* **70,** 2476–2486, doi:10.1175/JAS-D-12-0255.1.

Yokoi, S., M. Katsumata, and K. Yoneyama, 2014: Variability in surface meteorology and air-sea fluxes due to cumulus convective systems observed during CINDY/DYNAMO. *J. Geophys. Res. Atmos.,* **119,** 2064–2078, doi:10.1002/2013JD020621.

Yoneyama, K., C. Zhang, and C. N. Long, 2013: Tracking pulses of the Madden–Julian oscillation. *Bull. Amer. Meteor. Soc.,* **94,** 1871–1891, doi:10.1175/BAMS-D-12-00157.1.

Yu, L., and R. A. Weller, 2007: Objectively analyzed air–sea heat fluxes for the global ice-free oceans (1981–2005). *Bull. Amer. Meteor. Soc.,* **88,** 527–539, doi:10.1175/BAMS-88-4-527

Zhang, C., and M. J. McPhaden, 2000: Intraseasonal surface cooling in the equatorial western Pacific. *J. Climate,* **13,** 2261–2276, doi:10.1175/1520-0442(2000)013<2261:ISCITE>2.0.CO;2.

Zhang, Y. C., W. B. Rossow, A. A. Lacis, V. Oinas, and M. I. Mishchenko, 2004: Calculation of radiative fluxes from the surface to top of atmosphere based on ISCCP and other global data sets: Refinements of the radiative transfer model and the input data. *J. Geophys. Res.,* **109,** D19105, doi:10.1029/2003JD004457.